

Reconfigurable Intelligent Surfaces: A Signal Processing Perspective With Wireless Applications

Emil Björnson, Henk Wymeersch, Bho Matthiesen, Petar Popovski, Luca Sanguinetti, and
Elisabeth de Carvalho

Antenna array technology enables directional transmission and reception of wireless signals, for communications, localization, and sensing purposes. The signal processing algorithms that underpin this technology began to be developed several decades ago [1], but it is first with the ongoing deployment of the fifth-generation (5G) wireless mobile networks that it becomes a mainstream technology [2]. The number of antenna elements in the arrays of the 5G base stations and user devices can be measured at the order of 100 and 10, respectively. As the networks shift towards using higher frequency bands, more antennas fit into a given aperture. For communication purposes, the arrays are used to form beams in desired directions to improve the signal-to-noise ratio (SNR), multiplex data signals in the spatial domain (to one or multiple devices), and suppress interference by spatial filtering [2]. For localization purposes, these arrays are used to maintain the SNR when operating over wider bandwidths, for angle-of-arrival estimation, and to separate multiple sources and scatterers [3]. The practical use of these features requires that each antenna array is equipped with well-designed signal processing algorithms.

Looking beyond 5G, the advent of electromagnetic components that can shape how they interact with wireless signals enables a new dimension to be fine-tuned: the wireless propagation environment. A *reconfigurable intelligent surface (RIS)* is a two-dimensional surface of engineered material whose properties are reconfigurable rather than static [4]. For example, the scattering, absorption, reflection, and diffraction properties can be changed with time and controlled by software. In principle, the surface can be used to synthesize an arbitrarily-shaped object of the same size, when it comes to how electromagnetic waves interact with it [5]. As illustrated in Fig. 1, the surface consists of an array of discrete elements that can be controlled individually or on a group level. The key difference between an RIS and the common notion of an antenna array in 5G is that an RIS is neither part of the transmitter nor the receiver, but it is a

E. Björnson is with KTH Royal Institute of Technology, 100 44 Stockholm, Sweden (emilbjo@kth.se). H. Wymeersch is with Chalmers University of Technology, 412 96, Sweden (henkw@chalmers.se). B. Matthiesen is with University of Bremen, 28359 Bremen, Germany (matthiesen@uni-bremen.de). P. Popovski and E. de Carvalho are with Aalborg University, 9220 Aalborg, Denmark ({petarp,edc}@es.aau.dk). L. Sanguinetti is with University of Pisa, 56125 Pisa, Italy (luca.sanguinetti@unipi.it).

controllable part of the wireless propagation environment. The system-level role of an RIS is to influence the propagation of the wireless signals sent by other devices, without generating its own signals. It can be utilized to aid the communication within a wireless network by creating additional propagation paths, improving the properties of existing paths, and mitigating interference [6]. Moreover, it can be utilized for non-communication applications such as localization, sensing, and wireless power transfer [7], [8].

The long-term vision of the RIS technology is to create smart radio environments [9], where the wireless propagation conditions are co-engineered with the physical-layer signaling, and investigate how to utilize this new capability. The common protocol stack consists of seven layers and wireless technology is chiefly focused on the first three layers (physical, link, and network) [10]. An RIS operates at what can be referred to as Layer 0, where the traditional design issue is the antennas of the transmitter/receivers; one can think of RIS as extending the antenna design towards the environment, commonly seen as uncontrollable and decided by “nature”. This approach can profoundly change the wireless design beyond 5G.

This article provides a tutorial on the fundamental properties of the RIS technology from a signal processing perspective, to complement the recent surveys of electromagnetic and hardware aspects [4], [7], communication theory [11], and localization [8]. We will provide the formulas and derivations that are required to understand and analyze RIS-aided systems, and exemplify how they can be utilized for improved communication, localization, and sensing. We will also elaborate on the fundamentally new possibilities enabled by Layer 0 engineering and electromagnetic phenomena that remain to be modeled and utilized for improved signal processing.

I. HISTORY AND FUNDAMENTALS

RIS is an umbrella term that recently appeared in the communication field [12], but the technology has its roots in reconfigurable reflectarrays and metasurfaces in the electromagnetic field [4], [13]–[15]. There are several decades of research on how to build such surfaces and controlling their properties, and implementation concepts using different materials for different frequencies and use cases. The common feature is that the surface consists of many discrete elements with controllable properties, which are illustrated as colored squares in Fig. 1. The elements are nearly passive in the sense that the incoming signals are reradiated after “passive” analog filtering that cannot increase the power. Each element filters the signal by potentially reducing the amplitude, incurring time delays, and/or changing the polarization. The coloring in Fig. 1 exemplifies how the filtering in the individual elements cause different phase-shifts from $-\pi$ to π . The elements are designed to perform this filtering passively, but the key feature of an RIS is that the properties can be reconfigured over time by external stimuli, which is why it is called *nearly* passive. Fig. 1 illustrates how each element is controlled by a switch connected to a

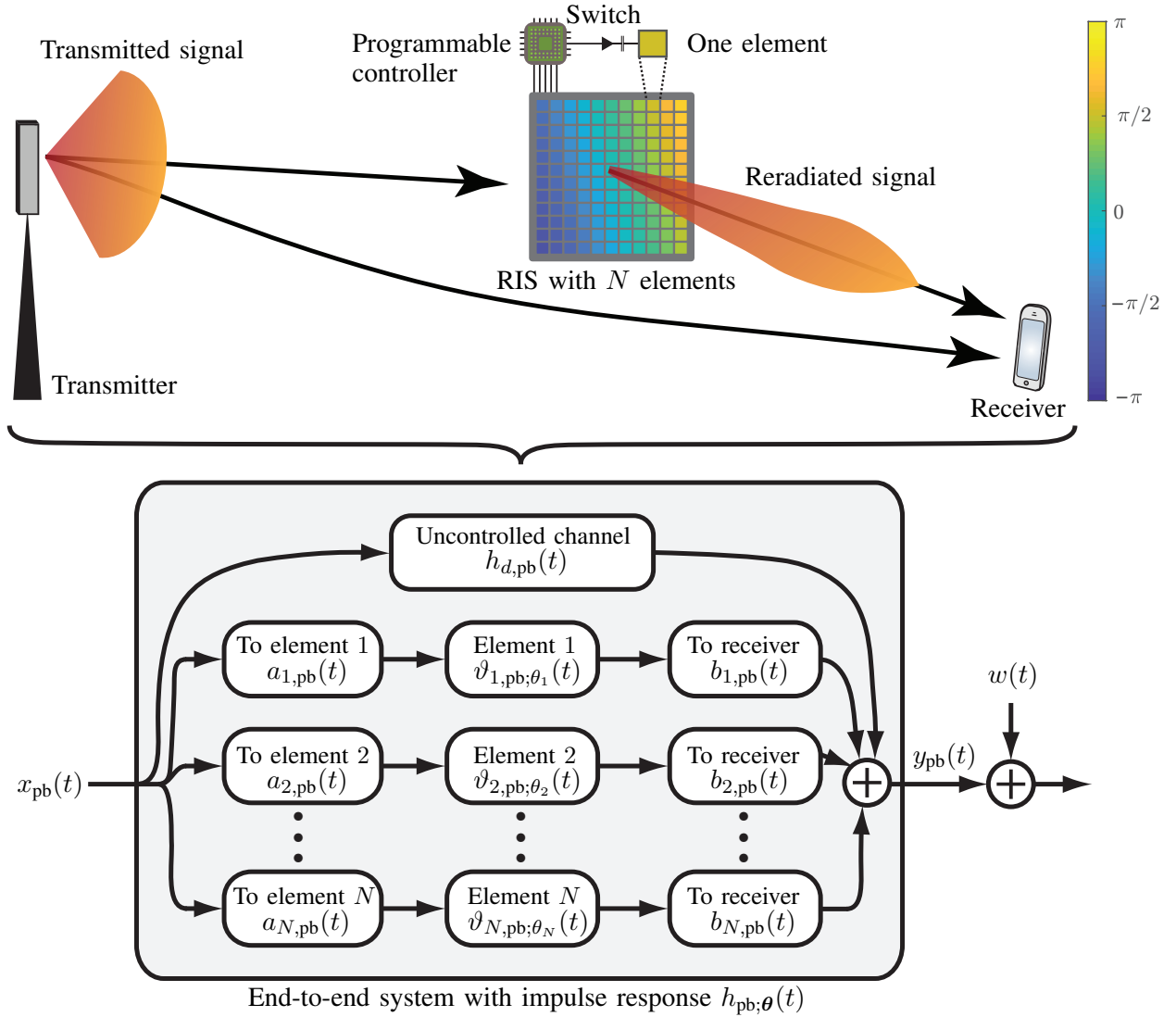


Fig. 1: Example of the wireless signaling from a transmitter to a receiver, where the signal both travels via an uncontrollable “direct” channel and via a controllable RIS with N elements. Each sub-wavelength-sized element filters the incident signal before it is reradiated. The controller configures the phase response of the filter, as illustrated by the coloring. The impulse response of the end-to-end channel consists of $N + 1$ chains of systems.

programmable controller. For instance, a varactor can be used to tune the impedance of the element, thereby controlling the reflection coefficient that determines the change in amplitude and phase of the reradiated signal [16]. The elements are typically sub-wavelength-sized (e.g., a square patch of size $\lambda/5 \times \lambda/5$) to behave as scatterers without a strong intrinsic directivity [17]. The RIS can then receive signals from any direction from the half-space towards which the RIS elements are facing and tune the pattern of reflection coefficients over the elements to reradiate signals with the desired direction and beam shape. We will later explain the signal processing algorithms that enable this type of operation.

The RIS technology appears under different names, such as software-controlled metasurfaces [6], intelligent reflecting surfaces [18], and a few others [2]. It should be viewed as a general concept for creating smart radio environments where the exact hardware characteristics have been abstracted away. However, it is likely that metasurfaces, where the elements are made of thin layers of metamaterial, will play a major role in practical implementations. Metamaterials have recently been successfully utilized for commercial antenna design in terrestrial and satellite communications (e.g., by Pivotal Commware and Kymeta), as well as radar (e.g., by Echodyne). The RIS technology is different in the sense that the surface is neither co-located with the transmitter nor with the receiver of the wireless signals, which opens the door for a variety of new use cases as well as new signal processing challenges regarding how to exploit the ability to control the channel. The new electromagnetic properties of RIS-aided systems require changes in the established models for discrete signal processing used in communications and localization, and create the need to reexamine the classical system models from first principles to ensure that the technology builds on a solid foundation. The objective of this paper is to provide such a foundation.

II. END-TO-END SYSTEM MODELING

To shed light on the fundamental RIS properties, we will begin by studying the basic setup in Fig. 1 in continuous time and derive the corresponding discrete-time models needed for digital signal processing.

A single-antenna transmitter sends a wireless passband signal $x_{\text{pb}}(t)$, with time index $t \in \mathbb{R}$, to a receiver via an RIS consisting of N scattering elements. We begin by considering the entire system as an uncontrollable black box; more precisely, it is modeled as linear and time-invariant (LTI) with the real-valued impulse response $h_{\text{pb}}(t)$. It then follows from standard signals-and-systems theory that the output signal $y_{\text{pb}}(t)$ is the convolution between the input and impulse response:

$$y_{\text{pb}}(t) = (h_{\text{pb}} * x_{\text{pb}})(t) = \int_{-\infty}^{\infty} h_{\text{pb}}(u)x_{\text{pb}}(t - u)du. \quad (1)$$

The characterizing feature of an RIS is that its properties can change with time. Hence, this LTI model can only be utilized for the duration of one configuration with a fixed impulse response $h_{\text{pb}}(t)$. We can distinguish between two RIS regimes: 1) *piecewise constant*, in which $h_{\text{pb}}(t)$ does not change while the signal of interest is non-zero, and 2) *continuously varying*, for which the LTI model in (1) is not valid. This tutorial focuses on the former category, where the LTI model can be used for the duration of one configuration, but we will briefly describe the second category when discussing mobility effects.

Suppose the transmitted signal is generated from a complex-valued baseband signal $x(t)$ with bandwidth $B/2$ that is modulated to the carrier frequency f_c , which satisfies $B \leq 2f_c$ and usually $B \ll f_c$. For

example, a typical scenario in 5G is $f_c = 3$ GHz and $B = 100$ MHz. The transmitted passband signal will then have bandwidth B and can be expressed as

$$x_{\text{pb}}(t) = \Re(\sqrt{2}x(t)e^{j2\pi f_c t}) = \frac{x(t)e^{j2\pi f_c t} + x^*(t)e^{-j2\pi f_c t}}{\sqrt{2}} \quad (2)$$

where $\Re(\cdot)$ outputs the real part of its argument, $j = \sqrt{-1}$ is the imaginary unit, and $\sqrt{2}$ keeps the power constant. If we let $\mathcal{F}_c\{\cdot\}$ denote the continuous Fourier transform, the relation in (2) is equivalent to

$$X_{\text{pb}}(f) = \frac{X(f - f_c) + X^*(-f - f_c)}{\sqrt{2}} \quad (3)$$

where $X_{\text{pb}}(f) = \mathcal{F}_c\{x_{\text{pb}}(t)\}$ and $X(f) = \mathcal{F}_c\{x(t)\}$ are the frequency-domain representations of the passband and baseband signals, respectively. The frequency response $H_{\text{pb}}(f) = \mathcal{F}_c\{h_{\text{pb}}(t)\}$ determines how the system filters different signal frequencies.

When analyzing passband systems in communication or localization, it is convenient to abstract away the carrier frequency and only consider the baseband signal $x(t)$, which, by definition, has the same power as $x_{\text{pb}}(t)$. We then need to find the counterpart to the input-output relation in (1) in the complex baseband. To this end, we define the received signal $y(t)$ in the complex baseband via $y_{\text{pb}}(t) = \Re(\sqrt{2}y(t)e^{j2\pi f_c t})$. By taking the Fourier transform of both sides of (1) and utilizing (3), we obtain

$$Y_{\text{pb}}(f) = H_{\text{pb}}(f) \frac{X(f - f_c) + X^*(-f - f_c)}{\sqrt{2}} = \frac{\overbrace{H_{\text{pb}}(f)X(f - f_c)}^{Y(f - f_c)} + \overbrace{H_{\text{pb}}^*(-f)X^*(-f - f_c)}^{Y^*(-f - f_c)}}{\sqrt{2}} \quad (4)$$

where we use the notation $Y_{\text{pb}}(f) = \mathcal{F}_c\{y_{\text{pb}}(t)\} = (Y(f - f_c) + Y^*(-f - f_c))/\sqrt{2}$ and $Y(f) = \mathcal{F}_c\{y(t)\}$. The last equality utilizes the property $H_{\text{pb}}(f) = H_{\text{pb}}^*(-f)$ for real-valued systems. From (4), we can identify the Fourier transform of the received baseband signal as

$$Y(f - f_c) = H_{\text{pb}}(f)X(f - f_c) \quad \Rightarrow \quad Y(f) = H_{\text{pb}}(f + f_c)X(f). \quad (5)$$

Taking the inverse Fourier transform of (5) yields

$$y(t) = (h * x)(t) = \int_{-\infty}^{\infty} h(u)x(t - u)du \quad (6)$$

where the impulse response $h(t) = h_{\text{pb}}(t)e^{-j2\pi f_c t}$ is a complex-baseband representation of the system. Since the system describes the wireless propagation environment, it can handle input signals with arbitrary frequency content. It is the passband signal $x_{\text{pb}}(t)$ that is downshifted to the complex-baseband signal $x(t)$. In general, $h_{\text{pb}}(t)$ will not be a passband filter and the passband property of the whole transmission is determined by the selection of the bandwidth B of $x(t)$. Thus, the downshifted $h(t)$ is generally not a baseband filter and we can vary the bandwidth B of the signal without changing the impulse response.

A. Continuous-time system model with RIS elements as reconfigurable filters

We will now look inside the system box in Fig. 1 and characterize the impulse response $h_{\text{pb};\boldsymbol{\theta}}(t)$ of the end-to-end channel from the transmitter to the receiver. We add the subscript $\boldsymbol{\theta} = [\theta_1, \dots, \theta_N]^T$ to indicate that the impulse response can be configured by a set of external control variables $\theta_1, \dots, \theta_N$ that will be defined below. We concentrate on the *controllable channel* via the RIS and omit the *uncontrollable channel*, which might include a line-of-sight (LOS) path and scattered paths not involving the RIS. We will add the latter part to the model later. For each of the N scattering elements of the RIS, the transmitted signal $x_{\text{pb}}(t)$ will propagate to it over an LTI channel represented by an arbitrary impulse response $a_{n,\text{pb}}(t)$ for element $n = 1, \dots, N$. If its frequency response is (approximately) constant over the passband used by the signal, we call it a narrowband channel. If it varies substantially, we call it a wideband channel. We will return to the modeling of wireless channels.

When the signal reaches element n , it will be filtered inside it and then reradiated. It all happens in the analog domain and we consider a passive operation that can be described by an LTI filter. The special RIS feature is that the impulse response $\vartheta_{n,\text{pb};\theta_n}(t)$ is reconfigurable in the sense that it is determined by an external stimulus represented by the variable θ_n . Depending on the RIS implementation, this control variable can take values in a discrete or continuous set. To be consistent with the LTI assumption, only one value can be utilized during the considered signal transmission and it is selected before the transmission is initiated. Since the element is much smaller than the wavelength, it can be modeled as a passive electric circuit. The passiveness also implies there is no added noise. There are other ways of operating an RIS that need to be modeled differently. For example, if we make the RIS operation dependent on the content of the impinging signal, we need to include noise since noiseless decoders are physically impossible.

Fig. 2 exemplifies the frequency response for the particular element circuit implementation considered in [19], where the capacitance can be tuned. We assume the intended carrier frequency is $f_c = 3$ GHz and since the frequency response is complex, we show the phase and amplitude responses for frequencies around the carrier. Fig. 2(a) shows the phase response for four different capacitance values, which have been selected to roughly give the phase-shifts $\pi/2, 0, -\pi/2, \pi$ at the carrier frequency. There are large phase variations over the GHz range, caused by having a frequency-dependent impedance and the fact that a constant time delay would result in a linearly varying phase-shift. However, we can approximate the phase response as constant if the signal bandwidth B is limited to a few tens of MHz. The frequency responses of wireless channels are usually only constant over a few hundreds of kHz, thus it is typically these channels that determine whether the end-to-end channel $h(t)$ is narrowband or wideband. The phase-shifts are caused by three phenomena. The curves in Fig. 2(a) begin close to $+\pi$ because the

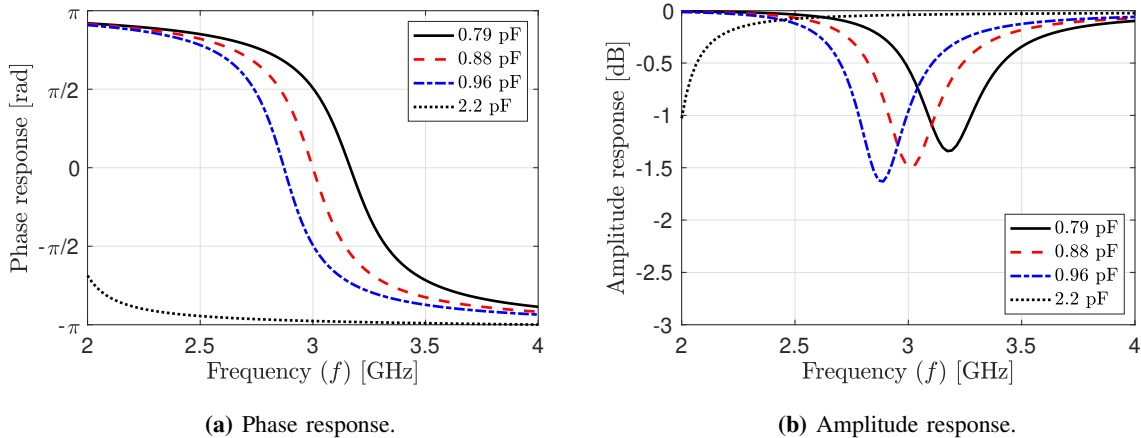


Fig. 2: Example of how the frequency response of an RIS element can be tuned by changing the effective capacitance using a varactor. The circuit model from [19, Eq. (4)] is used with 1 Ohm effective resistance and otherwise the same parameter values as in [19]. The four examples are selected to give equally spaced phase shifts at $f = 3$ GHz.

reradiated electric field is inverted. As f increases, a constant time delay leads to a larger phase-shift. Finally, the frequency-dependent impedance of the element also causes frequency-dependent time shifts.

The amplitude response is shown in Fig. 2(b) and reveals that the amplitude loss depends on both the frequency and capacitance. The losses are largest when tuning the RIS to achieve zero phase response due to resonance in the circuit. However, a few dB of signal losses in the RIS element is a minor issue compared to the propagation losses over wireless channels that can be at the order of 100 dB.

The signal that is reradiated from element n propagates to the receiver over an LTI channel with an arbitrary impulse response $b_{n,\text{pb}}(t)$. Since the transmitted signal propagates via element n over a cascade of three LTI filters, the joint impulse response is the convolution of their impulse responses: $(b_{n,\text{pb}} * \vartheta_{n,\text{pb};\theta_n} * a_{n,\text{pb}})(t)$. This happens for all the N elements, thus we obtain the input-output relation

$$y_{\text{pb}}(t) = \sum_{n=1}^N (b_{n,\text{pb}} * \vartheta_{n,\text{pb};\theta_n} * a_{n,\text{pb}} * x_{\text{pb}})(t) = \underbrace{\left(\left[\sum_{n=1}^N b_{n,\text{pb}} * \vartheta_{n,\text{pb};\theta_n} * a_{n,\text{pb}} \right] * x_{\text{pb}} \right)}_{=h_{\text{pb};\theta}}(t). \quad (7)$$

From (7), we can identify the impulse response of the end-to-end system as

$$h_{\text{pb};\theta}(t) = \sum_{n=1}^N (b_{n,\text{pb}} * \vartheta_{n,\text{pb};\theta_n} * a_{n,\text{pb}})(t). \quad (8)$$

We can transform the passband system in (7) to an equivalent complex baseband representation using (6):

$$y(t) = \sum_{n=1}^N (b_n * \vartheta_{n;\theta_n} * a_n * x)(t) \quad (9)$$

where $a_n(t) = a_{n,\text{pb}}(t)e^{-j2\pi f_c t}$, $b_n(t) = b_{n,\text{pb}}(t)e^{-j2\pi f_c t}$, and $\vartheta_{n;\theta_n}(t) = \vartheta_{n,\text{pb};\theta_n}(t)e^{-j2\pi f_c t}$ are the channels and filter associated with element n . The end-to-end channel has impulse response $h_{\theta}(t) =$

$\sum_{n=1}^N (b_n * \vartheta_{n;\theta_n} * a_n)(t)$. While complex baseband representations are commonly appearing in textbooks, the definitions can vary slightly; particularly, when it comes to scaling factors and how the baseband-equivalent impulse responses are defined. We have selected a specific set of definitions for which the convolution between impulse responses in the passband becomes a convolution between the corresponding impulse responses in the complex baseband, without the appearance of additional scaling factors.

B. Equivalent discrete-time system model

In both localization and communication, the continuous-time complex baseband signal $x(t)$ is usually generated to represent a complex discrete-time signal $x[m]$, where m is the integer index, via pulse-amplitude modulation (PAM). Recall that the baseband bandwidth is $B/2$. We consider ideal PAM using a unit-energy sinc-pulse $p(t) = \sqrt{B}\text{sinc}(Bt)$ and the symbol rate B , for which

$$x(t) = \sum_{m=-\infty}^{\infty} x[m]p\left(t - \frac{m}{B}\right). \quad (10)$$

Since the actual input signal $x[m]$ is in discrete time, it is convenient to abstract away the entire continuous-time description by sampling the received signal to obtain an end-to-end discrete-time system model. Before sampling, we must add the thermal receiver noise and lowpass filtering at the receiver into the model. We model the noise by a white circularly symmetric complex Gaussian random process $w(t)$ with power-spectral density N_0 . Adding it to the received signal in (6) as $z(t) = y(t) + w(t)$, we obtain

$$z(t) = (h_{\theta} * x)(t) + w(t) = \sum_{m=-\infty}^{\infty} x[m](h_{\theta} * p)\left(t - \frac{m}{B}\right) + w(t) \quad (11)$$

where the equality follows from (10). Since the desired signal is bandlimited to $|f| \leq B/2$, while the noise is not, we filter $z(t)$ at the receiver using an ideal lowpass filter with impulse response $p(t)$, same as the pulse in (10), to remove the out-of-band noise. We can then take samples at the symbol rate, at time instants $t = k/B + \eta$ where k is the integer sample index and η is a common delay, to obtain

$$z[k] = (p * z)(t) \Big|_{t=k/B+\eta} = \sum_{m=-\infty}^{\infty} x[m]h_{\theta}[k-m] + w[k] \quad (12)$$

where the discrete-time impulse response is defined as

$$h_{\theta}[k] = (p * h_{\theta} * p)(t) \Big|_{t=k/B+\eta} = \sum_{n=1}^N (p * b_n * \vartheta_{n;\theta_n} * a_n * p)(t) \Big|_{t=k/B+\eta} \quad (13)$$

by inserting the RIS system model from (9). Note that the discrete-time impulse response is created by lowpass filtering of the end-to-end continuous-time impulse response $h_{\theta}(t)$ and then taking samples of it. The discrete-time noise $w[k]$ in (12) can be shown to be circularly symmetric complex Gaussian distributed and independent for different k :

$$w[k] = (p * w)(t) \Big|_{t=k/B+\eta} \sim \mathcal{N}_{\mathbb{C}}(0, N_0). \quad (14)$$

The discrete-time model in (12) applies to any system but can be simplified by considering the specific properties that wireless channels and practical signals possess: a) The channels are causal and incur a finite maximum delay; b) The ideal pulse function $p(t)$ is approximated by something causal and time-limited. This implies that the channel is a finite impulse response (FIR) filter with $M \geq 1$ terms:

$$z[k] = \sum_{m=k-M+1}^k x[m]h_{\theta}[k-m] + w[k] = \sum_{\ell=0}^{M-1} h_{\theta}[\ell]x[k-\ell] + w[k] \quad (15)$$

where $h_{\theta}[0], \dots, h_{\theta}[M-1]$ are the non-zero components of the impulse response.

C. Canonical multicarrier system model

The discrete-time system model in (15) describes a dispersive channel with a memory of $M-1$ previous symbols; that is, the received $z[k]$ contains not only the currently transmitted signal $x[k]$ but also intersymbol interference from $x[k-1], \dots, x[k-M+1]$. A common way to untangle the interference is to design the transmitted symbols using orthogonal frequency-division multiplexing (OFDM), transforming the channel into a collection of separate frequency subcarriers. We will provide the corresponding reformulated system model, which will be utilized for both communication and localization.

Suppose we want to transmit a block of K symbols, $\chi[0], \dots, \chi[K-1]$, and append a so-called cyclic prefix to obtain the following sequence of length $K+M-1$ that can be transmitted over (15):

$$x[k] = \begin{cases} \chi[k] & k = 0, \dots, K-1 \\ \chi[k+K] & k = -M+1, \dots, -1. \end{cases} \quad (16)$$

Since we added the last $M-1$ symbols as a prefix, we can interpret (15) as a cyclic convolution between $\{\chi[k] : k = 0, \dots, K-1\}$ and $\{h_{\theta}[k] : k = 0, \dots, M-1\}$, plus noise, if $K > M$. Let us define the K -point discrete Fourier transform (DFT) of an arbitrary sequence $s[k]$ as $\mathcal{F}_d\{s[k]\} = \frac{1}{\sqrt{K}} \sum_{k=0}^{K-1} s[k]e^{-j2\pi k\nu/K}$, where the scaling factor keeps the energy constant. Taking the discrete Fourier transform of (15) and utilizing that cyclic convolution becomes the product of the corresponding Fourier transforms, we obtain

$$\bar{z}[\nu] = \bar{h}_{\theta}[\nu]\bar{x}[\nu] + \bar{w}[\nu], \quad \nu = 0, \dots, K-1 \quad (17)$$

where $\bar{z}[\nu] = \mathcal{F}_d\{z[k]\}$ and $\bar{x}[\nu] = \mathcal{F}_d\{x[k]\}$ describe the received and transmitted signals, respectively, in the frequency domain. This equation describes K subcarriers. At the ν th subcarrier, the frequency response of the end-to-end channel is

$$\bar{h}_{\theta}[\nu] = \sum_{k=0}^{M-1} h_{\theta}[k]e^{-j2\pi k\nu/K} \quad (18)$$

and the transformed noise $\bar{w}[\nu] = \mathcal{F}_d\{w[k]\} \sim \mathcal{N}_{\mathbb{C}}(0, N_0)$ is independent for $\nu = 0, \dots, K-1$.

Notice that (17) has a more convenient structure than (15) since there is no intersymbol interference. It is known as a discrete memoryless channel with additive white Gaussian noise (AWGN). OFDM exploits this feature by treating $\bar{x}[\nu]$ as the transmitted signal and $\bar{z}[\nu]$ as the received signal. In an OFDM implementation, the transmitted time-domain $x[k]$ is generated from $\bar{x}[\nu]$ by an inverse Fourier transform, while the receiver computes the Fourier transform of its received signal $z[k]$ to obtain $\bar{z}[\nu]$.

D. Example of multipath channels

We will now give a concrete example of how the end-to-end channel $\bar{h}_\theta[\nu]$ in the OFDM system model (17) is determined by the propagation channels and RIS elements. Suppose the channel from the transmitter to the n th RIS element consists of L_a propagation paths, then the impulse response is modeled as

$$a_{n,\text{pb}}(t) = \sum_{l=1}^{L_a} \sqrt{\alpha_n^l} \delta(t - \tau_{n,a}^l) \quad \Rightarrow \quad a_n(t) = \sum_{l=1}^{L_a} \sqrt{\alpha_n^l} e^{-j2\pi f_c t} \delta(t - \tau_{n,a}^l) \quad (19)$$

where $\alpha_n^l \in [0, 1]$ is the propagation loss and $\tau_{n,a}^l \geq 0$ is the delay of the l th path, while $\delta(t)$ denotes the Dirac delta function. Similarly, suppose there are L_b propagation paths from the n th RIS element to the receiver, then the impulse response can be modeled as

$$b_{n,\text{pb}}(t) = \sum_{\ell=1}^{L_b} \sqrt{\beta_n^\ell} \delta(t - \tau_{n,b}^\ell) \quad \Rightarrow \quad b_n(t) = \sum_{\ell=1}^{L_b} \sqrt{\beta_n^\ell} e^{-j2\pi f_c t} \delta(t - \tau_{n,b}^\ell) \quad (20)$$

where $\beta_n^\ell \in [0, 1]$ is the propagation loss and $\tau_{n,b}^\ell \geq 0$ is the delay of the ℓ th path. We assume the signal bandwidth is sufficiently small to make the frequency response of the RIS element constant (recall Fig. 2); that is, the RIS is narrowband while the wireless channels might be wideband. For a given configuration $\theta_n \in \Omega$, selected from some set Ω of feasible configurations, element n is reradiating a fraction $\gamma_{\theta_n} \in [0, 1]$ of the incident signal power and incurs a delay of $\tau_{\theta_n} \geq 0$, so that

$$\vartheta_{n,\text{pb};\theta_n}(t) = \sqrt{\gamma_{\theta_n}} \delta(t - \tau_{\theta_n}) \quad \Rightarrow \quad \vartheta_{n;\theta_n}(t) = \sqrt{\gamma_{\theta_n}} e^{-j2\pi f_c t} \delta(t - \tau_{\theta_n}). \quad (21)$$

Under these assumptions, the discrete-time impulse response in (13) particularizes to

$$h_\theta[k] = \sum_{n=1}^N \sum_{l=1}^{L_a} \sum_{\ell=1}^{L_b} \sqrt{\alpha_n^l \beta_n^\ell \gamma_{\theta_n}} e^{-j2\pi f_c (\tau_{n,a}^l + \tau_{n,b}^\ell + \tau_{\theta_n})} \underbrace{\text{sinc}(k + B(\eta - \tau_{n,a}^l - \tau_{n,b}^\ell - \tau_{\theta_n}))}_{\approx \text{sinc}(k + B(\eta - \tau_{n,a}^l - \tau_{n,b}^\ell))} \quad (22)$$

where the approximation utilizes the fact that the delay in the RIS is much smaller than the propagation delays, so its impact on the symbol rate is negligible: $B\tau_{\theta_n} \approx 0$. However, since $f_c \gg B$, the RIS creates phase-shifts $2\pi f_c \tau_{\theta_n}$ in (22) that are substantial (within a few periods of 2π), as illustrated in Fig. 2(a).

We notice from (22) that there are NL_aL_b paths from the transmitter to the receiver, each having a unique propagation loss $\alpha_n^l \beta_n^\ell \gamma_{\theta_n}$ which is the product of the losses between the transmitter to an RIS

element, inside the element, and from the element to the receiver. Due to the product operation, each path is very weak but the large number of paths can potentially lead to a good SNR. Each path is also associated with a phase-shift $e^{-j2\pi f_c(\tau_{n,a}^l + \tau_{n,b}^\ell + \tau_{\theta_n})}$ containing the accumulated delays. The sinc-function determines how the signal energy carried by the path is divided between the M taps of the FIR filter.

The frequency response $\bar{h}_\theta[\nu]$ can now be computed using (18). To obtain a compact expression, we first notice that (22) can be expressed as an inner product of two vectors:

$$h_\theta[k] = \underbrace{\begin{bmatrix} \sum_{l=1}^{L_a} \sum_{\ell=1}^{L_b} \sqrt{\alpha_1^l \beta_1^\ell} e^{-j2\pi f_c(\tau_{1,a}^l + \tau_{1,b}^\ell)} \text{sinc}(k + B(\eta - \tau_{1,a}^l - \tau_{1,b}^\ell)) \\ \vdots \\ \sum_{l=1}^{L_a} \sum_{\ell=1}^{L_b} \sqrt{\alpha_N^l \beta_N^\ell} e^{-j2\pi f_c(\tau_{N,a}^l + \tau_{N,b}^\ell)} \text{sinc}(k + B(\eta - \tau_{N,a}^l - \tau_{N,b}^\ell)) \end{bmatrix}}_{\mathbf{v}_k^T} \cdot \underbrace{\begin{bmatrix} \sqrt{\gamma_{\theta_1}} e^{-j2\pi f_c \tau_{\theta_1}} \\ \vdots \\ \sqrt{\gamma_{\theta_N}} e^{-j2\pi f_c \tau_{\theta_N}} \end{bmatrix}}_{\boldsymbol{\omega}_\theta}. \quad (23)$$

The propagation channels determine $\mathbf{v}_k \in \mathbb{C}^N$, while the RIS determines $\boldsymbol{\omega}_\theta \in \mathbb{C}^N$ and it is the same for all k . Hence, \mathbf{v}_k is given by nature while $\boldsymbol{\omega}_\theta$ is controllable. We can compute the frequency response as

$$\underbrace{\begin{bmatrix} \bar{h}_\theta[0] \\ \vdots \\ \bar{h}_\theta[K-1] \end{bmatrix}}_{\bar{\mathbf{h}}_\theta} = \mathbf{F} \underbrace{\begin{bmatrix} h_\theta[0] \\ \vdots \\ h_\theta[M-1] \end{bmatrix}}_{\mathbf{h}} = \mathbf{F} \mathbf{V}^T \boldsymbol{\omega}_\theta \quad (24)$$

where $\mathbf{V} = [\mathbf{v}_0, \dots, \mathbf{v}_{M-1}]$ is an $N \times M$ matrix and \mathbf{F} is a $K \times M$ DFT matrix with the (ν, k) th element being $e^{-j2\pi k\nu/K}$. We will make use of this notation when considering wideband systems.

E. Simplified narrowband system model

In some communication applications, the delay spread of the different paths is so small that we achieve an impulse response with only one strong tap. Suppose we can synchronize the transmitter and receiver by selecting the sampling delay η to make $B(\eta - \tau_{n,a}^l - \tau_{n,b}^\ell) \approx 0$ for all l, ℓ , and n . This is achievable when the delay spread is much smaller than the sampling period $1/B$. Since the individual propagation paths are not distinguishable anymore, we can set $L_a = L_b = 1$ without loss of generality. By omitting the superscripts with path indices, we can approximate the impulse response in (22) as

$$h_\theta[k] \approx \sum_{n=1}^N \sqrt{\alpha_n \beta_n \gamma_{\theta_n}} e^{-j2\pi f_c(\tau_{n,a} + \tau_{n,b} + \tau_{\theta_n})} \text{sinc}(k) = \begin{cases} \sum_{n=1}^N \sqrt{\alpha_n \beta_n \gamma_{\theta_n}} e^{-j2\pi f_c(\tau_{n,a} + \tau_{n,b} + \tau_{\theta_n})} & k = 0 \\ 0 & k \neq 0. \end{cases} \quad (25)$$

A channel of this kind is called narrowband and the input-output system in (12) simplifies to

$$z[k] = h_\theta[0]x[k] + w[k] = \sum_{n=1}^N \sqrt{\alpha_n \beta_n \gamma_{\theta_n}} e^{-j2\pi f_c(\tau_{n,a} + \tau_{n,b} + \tau_{\theta_n})} x[k] + w[k]. \quad (26)$$

This is a popular special case where there is no need for OFDM since there is no intersymbol interference.

III. RIS-AIDED COMMUNICATIONS

The central element when characterizing the performance of a communication channel is the probabilistic relation between the discrete-time input x and output z , specified by the conditional probability density function (PDF) $p(z|x)$. For example, the narrowband system in (26) has the complex symbols x and z as inputs and outputs, respectively. The received signal for the k th transmitted symbol is

$$z[k] = h_{\theta} x[k] + w[k], \quad k = 0, 1, \dots \quad (27)$$

where a discrete sequence $\{x[k]\}$ of codeword symbols describing the payload data is transmitted and each one is attenuated by a factor $h_{\theta} \in \mathbb{C}$ and corrupted by the independent noise $w[k] \sim \mathcal{N}_{\mathbb{C}}(0, N_0)$. To arrive at the well-known communication model of an AWGN channel, we need some additional assumptions. First, h_{θ} is fixed for all transmitted symbols that belong to a given codeword, and its value is known to the transmitter and receiver. Second, we assume that the power limit of the sender is P Watt. Since there are B symbols per second, this implies each symbol should satisfy the power constraint $\mathbb{E}\{|x[k]|^2\} \leq P/B$. Finally, we need to assume that the transmitter knows the SNR of the channel, given by $\text{SNR} = P|h_{\theta}|^2/(BN_0)$. The capacity of this channel is

$$C = B \log_2(1 + \text{SNR}) = B \log_2 \left(1 + \frac{P|h_{\theta}|^2}{BN_0} \right) \quad \text{bit/s.} \quad (28)$$

If any of the above assumptions are violated (e.g., h_{θ} is not known by the receiver or the SNR is not known by the transmitter), the channel is not AWGN and the capacity formula (28) is not valid. For a deeper discussion on how assumptions affect the definition of a communication channel, see [10, Ch. 6].

This discussion can be extrapolated to the OFDM channel in (17), obtained as a superposition of K parallel memoryless AWGN channels. In this case, we need to consider a set of K channel values $\{\bar{h}_{\theta}[\nu]\}$, each of them associated with one of the narrowband subcarrier channels.

Given the transmitter, the receiver, and a narrowband channel, an obvious objective of an RIS would be to select the configuration θ to create a channel h_{θ} that maximizes the capacity (28). More generally, in case of OFDM, the objective is to create a set of K channels $\{\bar{h}_{\theta}[\nu]\}$ that maximizes the sum of the capacity of the constituent subcarrier channels. In this case, the values of the channels $\bar{h}_{\theta}[0], \dots, \bar{h}_{\theta}[K-1]$ may not be independently optimized, as they are determined by the same RIS configuration.

Following the assumptions of AWGN channels, it is important to note that the RIS-controlled channel in (27) is created before the actual communication starts with the first symbol of a codeword at, say, $k = 0$. This can be achieved by an *out-of-band control channel* that sends information that configures the RIS elements. The term “out-of-band” should be understood in the way that the control information does not consume part of the useful bandwidth B . This can be achieved, for example, by a dedicated control channel towards the RIS that uses different frequency spectrum than the one associated with (27).

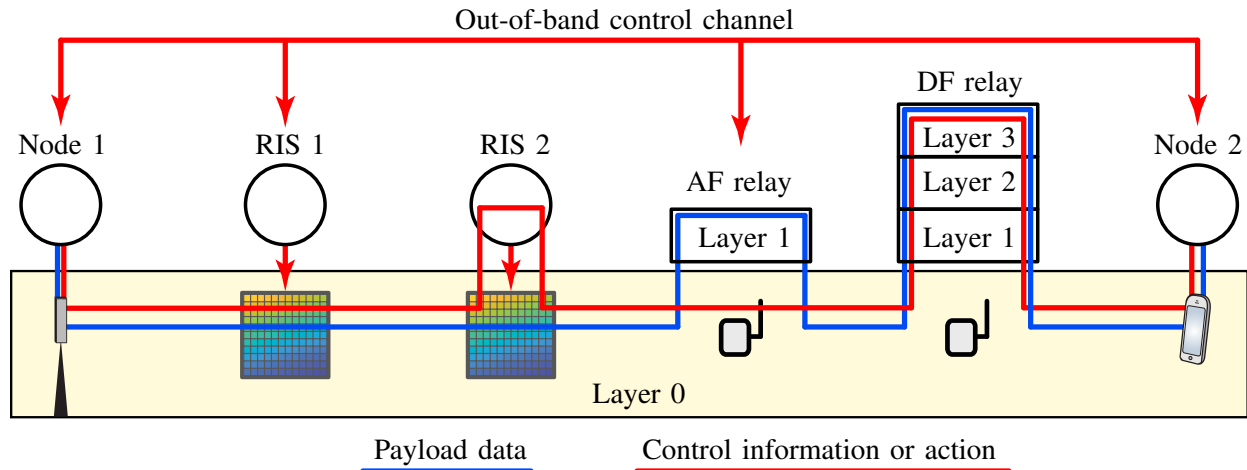


Fig. 3: A layered perspective on RIS and relay functionality. The wireless connection between Node 1 and Node 2 is supported by a cascade of RIS 1 with out-of-band control, RIS 2 with in-band control, AF relay and DF relay.

Alternatively, an *in-band control channel* can be used. It consumes part of the useful bandwidth to configure the RIS. This can still be used to obtain the AWGN channel model in (27), provided that the in-band control information has been sent before the transmission of the symbol at $k = 0$.

In principle, it is also possible to use an in-band control channel in which the information for controlling the RIS operation is sent simultaneously with the payload data. In this case, the RIS should be able to decode the control information embedded into $x[k]$ and based on that, causally change the value of h_θ (i.e., change θ) for symbols with indices $j > k$. One thing that is immediately clear is that the end-to-end channel cannot be an AWGN channel anymore. In an information-theoretic sense, this situation corresponds to a relay channel in which the source broadcasts two types of data: payload data (intended for the receiver) and control data (intended for the RIS that becomes a relay node). Based on the received data, the RIS changes the configuration of the end-to-end channel.

The works [5], [20], [21] compare RIS-aided and traditional relay-aided systems. Here we provide a different perspective, using the layering framework, as depicted in Fig. 3. We consider a wireless connection between Node 1 and Node 2, aided by a cascade of RISs and relays. Nodes 1 and 2 implement all protocol layers (not depicted). Suppose Node 1 transmits to Node 2. The wireless signal goes through RIS 1, which is configured using an out-of-band control channel. The payload data (blue line) stays at Layer 0, meaning that RIS only affects the propagation environment without processing the communication flow. The control information (red line) shows that there needs to be an out-of-band communication between Node 1, Node 2, and RIS 1 to select a suitable configuration θ . Next, the signal passes through RIS 2, which uses an in-band control channel. The payload data stays at Layer 0, while

the RIS controller decodes the control information and adapts its configuration. Next, the signal proceeds through a non-regenerative amplify-and-forward (AF) relay. The payload data goes through Layer 1 (physical) where the signal is amplified and the active circuitry introduces additional noise. The depicted control channel is out-of-band but, similar to the RIS 1 case, it can be implemented in-band, using a dedicated communication protocol that is not used by the payload data. Finally, the decode-and-forward (DF) relay decodes both payload and control data, and is capable to interpret the control information.

A. RIS design for narrowband capacity maximization

To explain how an RIS can be used to maximize the capacity, we begin by considering a simple setup: a single-antenna transmitter communicates with a single-antenna receiver over a narrowband channel. We further assume that the RIS elements can be perfectly configured: we can select $\tau_{\theta_n} \geq 0$ so that $2\pi f_c \tau_{\theta_n}$ can take any value between 0 and 2π for $n = 1, \dots, N$, while the amplitude response is constant $\gamma_{\theta_n} = \gamma$.

The considered system is a memoryless AWGN channel with $h_{\theta} = \sum_{n=1}^N \sqrt{\alpha_n \beta_n} \gamma e^{-j2\pi f_c (\tau_{n,a} + \tau_{n,b} + \tau_{\theta_n})}$, thus the capacity in (28) becomes $B \log_2(1 + \text{SNR})$ with

$$\begin{aligned} \text{SNR} &= \frac{P}{BN_0} \left| \sum_{n=1}^N \sqrt{\alpha_n \beta_n} \gamma e^{-j2\pi f_c (\tau_{n,a} + \tau_{n,b} + \tau_{\theta_n})} \right|^2 \\ &= \frac{P}{BN_0} \left[\begin{array}{c} \sqrt[4]{\alpha_1 \beta_1} \gamma_{\theta_1} \\ \vdots \\ \sqrt[4]{\alpha_N \beta_N} \gamma \end{array} \right]^T \left[\begin{array}{c} e^{-j2\pi f_c (\tau_{1,a} + \tau_{1,b} + \tau_{\theta_1})} \sqrt[4]{\alpha_1 \beta_1} \gamma_{\theta_1} \\ \vdots \\ e^{-j2\pi f_c (\tau_{N,a} + \tau_{N,b} + \tau_{\theta_N})} \sqrt[4]{\alpha_N \beta_N} \gamma \end{array} \right] \quad (29) \end{aligned}$$

$$\leq \frac{P}{BN_0} \left| \sum_{n=1}^N \sqrt{\alpha_n \beta_n} \gamma \right|^2 \quad (30)$$

where the last step follows from the Cauchy-Schwartz inequality. The upper bound in that inequality is achieved if and only if the two vectors in (29) are parallel, which occurs when $e^{-j2\pi f_c (\tau_{n,a} + \tau_{n,b} + \tau_{\theta_n})}$ is the same for all n [22]. Hence, each RIS element should delay its reradiated signal so that it reaches the receiver time-synchronously with the signals from all the other RIS elements. The solution that achieves this effect with minimum overall delay is [23]

$$\tau_{\theta_n} = \left(\max_{i=1, \dots, N} \tau_{i,a} + \tau_{i,b} \right) - \tau_{n,a} - \tau_{n,b} \quad (31)$$

where $\tau_{\theta_n} = 0$ for the element experiencing the largest propagation delay, while all other elements add positive delays $\tau_{\theta_n} > 0$ to match the largest propagation delay.

Suppose all N paths have the same propagation loss: $\alpha_n \beta_n = \alpha \beta$. This is a common property when the RIS is in the far-field of the transmitter and receiver. It then follows that $|\sum_{n=1}^N \sqrt{\alpha_n \beta_n} \gamma|^2 = N^2 \alpha \beta \gamma$, thus the SNR grows quadratically with the number of RIS elements [22]. The intuition behind this result is

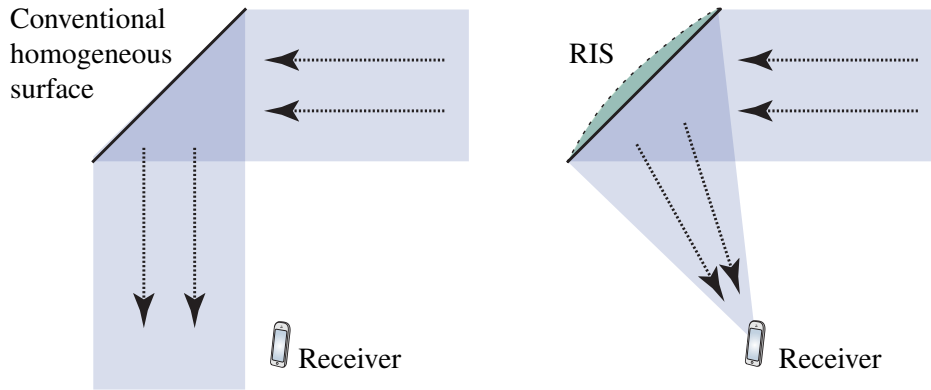


Fig. 4: A large homogeneous flat surface will reflect an incident plane wave in another direction, determined by Snell’s law. In contrast, an RIS of the same physical dimensions can be configured to synthesize the shape of a different object (here: a parabolic reflector), thereby controlling the direction and shape of the reflected waveform.

that the surface intercepts signal energy proportional to N (i.e., proportional to its area) and then focuses the reradiated signals to increase the received signal energy proportional to N (thanks to constructive interference of the signals from the N elements). This result indicates that a physically large RIS is much more effective than a small RIS, which is fundamentally important since N^2 is multiplied with $\alpha\beta$, which is the product of two pathlosses that both can be very small numbers.

A geometrical interpretation of the optimal RIS configuration is provided in Fig. 4, where a plane wave is incident on a large flat surface. If it is a homogeneous metal surface, as shown to the left, the plane wave changes direction according to Snell’s law but otherwise be unaffected (e.g., two rays remain parallel). Each point on the surface reradiates the incident signal without causing any extra delays. In the illustrated scenario, the reflected signal does not reach the receiver. If the surface is replaced by an RIS, as shown to the right, the optimized configuration focuses the reradiated signal at the receiver. The configuration in (31) adds extra delays in the center of the surface to make the propagation time to the receiver equal for all parallel rays that are reflected. As illustrated by the dashed line, the RIS is synthesizing how signals would have been reflected by a parabolic surface, where the length of each path via the surface is equal. This configuration will both change the shape and the main direction of the waveform (e.g., two parallel incident rays have different directions when reradiated). The same effect could have been mechanically achieved by rotating and bending the flat metal surface, but doing it electronically using an RIS adds great flexibility since different surface shapes can be synthesized at different times.

B. Narrowband capacity maximization with a partially uncontrollable channel

In practice, there are likely propagation paths between the transmitter and the receiver that are not involving the RIS, thus outside its control. Recall from Fig. 1 that these paths constitute the uncontrollable

channel, which has impulse response $h_{d,\text{pb}}(t)$. For a narrowband system, the uncontrollable channel can be represented in the discrete-time complex baseband by an impulse response $\sqrt{\rho}e^{-j2\pi f_c \tau_d}$, where $\rho \in [0, 1]$ is the propagation loss and $\tau_d \geq 0$ is the delay. We then obtain a memoryless AWGN channel with $h_{\theta} = \sqrt{\rho}e^{-j2\pi f_c \tau_d} + \sum_{n=1}^N \sqrt{\alpha_n \beta_n \gamma} e^{-j2\pi f_c (\tau_{n,a} + \tau_{n,b} + \tau_{\theta_n})}$, for which the capacity in (28) becomes $B \log_2(1 + \text{SNR})$ with

$$\begin{aligned} \text{SNR} &= \frac{P}{BN_0} \left| \sqrt{\rho}e^{-j2\pi f_c \tau_d} + \sum_{n=1}^N \sqrt{\alpha_n \beta_n \gamma} e^{-j2\pi f_c (\tau_{n,a} + \tau_{n,b} + \tau_{\theta_n})} \right|^2 \\ &\leq \frac{P}{BN_0} \left| \sqrt{\rho}e^{-j2\pi f_c \tau_d} + \sum_{n=1}^N \sqrt{\alpha_n \beta_n \gamma} e^{-j2\pi f_c \tau_d} \right|^2 = \frac{P}{BN_0} \left| \sqrt{\rho} + \sum_{n=1}^N \sqrt{\alpha_n \beta_n \gamma} \right|^2. \end{aligned} \quad (32)$$

The upper bound is once again obtained by the Cauchy-Schwartz inequality, with the key difference that we cannot control the phase of the uncontrollable channel component. Hence, we need to select the delays of the RIS elements so that the N reradiated signals reach the receiver in phase with the signal over the uncontrollable channel. Note that $e^{-j2\pi f_c \tau_d} = e^{-j2\pi f_c (\tau_{n,a} + \tau_{n,b} + \tau_{\theta_n})}$ holds if $\tau_{\theta_n} = \tau_d - \tau_{n,a} - \tau_{n,b}$ for $n = 1, \dots, N$, but this results in a negative delay if the uncontrollable channel path is shorter than the paths via the RIS, which is usually the case. Hence, to achieve a causal system implementation, we need to select the delays as $\tau_{\theta_n} = (\tau_d - \tau_{n,a} - \tau_{n,b}) + \frac{k_n}{f_c}$ where k_n is an integer such that $\tau_{\theta_n} \geq 0$; that is, $k_n \geq \lceil f_c (\tau_{n,a} + \tau_{n,b} - \tau_d) \rceil$, where $\lceil \cdot \rceil$ is the ceiling function. The delay spread T_d in this scenario is

$$T_d = \max_{i=1, \dots, N} \{ \tau_{i,a} + \tau_{i,b} + \tau_{\theta_i} \} - \tau_d = \max_i \left\{ \frac{k_i}{f_c} \right\} \geq \max_i \left\{ \frac{1}{f_c} \lceil f_c (\tau_{i,a} + \tau_{i,b} - \tau_d) \rceil \right\} \quad (33)$$

Hence, the delay spread is minimized for the smallest allowed k_n [23]: $k_{n,\min} = \lceil f_c (\tau_{n,a} + \tau_{n,b} - \tau_d) \rceil$.

The jointly SNR- and delay-optimal configuration of the RIS is

$$\tau_{\theta_n} = (\tau_d - \tau_{n,a} - \tau_{n,b}) + \frac{k_{n,\min}}{f_c}. \quad (34)$$

The upper bound in (32) is achieved when the RIS configuration θ can be selected from a continuous set. Suppose the RIS hardware restricts us to select τ_{θ_n} from a discrete set such that $2\pi f_c \tau_{\theta_n} \in \{\pi/2, 0, -\pi/2, -\pi\}$, as exemplified in Fig. 2. The capacity maximization is now a combinatorial problem with 4^N possible configurations. Evaluating all options is computationally very complex, but a good heuristic is to rotate each term $e^{-j2\pi f_c (\tau_{n,a} + \tau_{n,b} + \tau_{\theta_n})}$ so it is as close to $e^{-j2\pi f_c \tau_d}$ as possible on the unit circle. This leads to a partially coherent addition of the $N + 1$ components of the channel h_{θ} . One can prove that the SNR loss is only around $8/\pi^2 = -0.9$ dB when having these four configurations [24], which implies that a small number of configurations per element is sufficient when implementing an RIS.

Fig. 5 shows the capacities that can be achieved in a narrowband setup with $B = 1$ MHz and a varying number of RIS elements with $\gamma = 1$. The propagation losses via the RIS are $\alpha_n = -80$ dB and

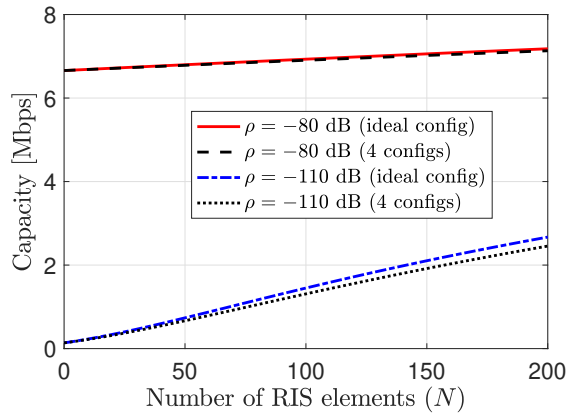


Fig. 5: The capacity of a narrowband channel grows with the number of RIS elements. The benefit of controlling the channel using an RIS is particularly large when the uncontrollable “direct” channel is weak.

$\beta_n = -60$ dB, while $P/(BN_0) = 100$ dB. We consider two cases for the uncontrollable channel: -80 dB (strong) and -110 dB (weak). We notice that the RIS can increase the capacity by orders-of-magnitude when the uncontrollable channel is weak. The RIS-controlled path is 30 dB weaker when $N = 1$, but since its contribution to the SNR grows as N^2 , it surpasses the uncontrollable channel in strength when having $N = 32$ elements and beyond that, the SNR grows as N^2 . When the uncontrollable channel is strong, the capacity is already high and the RIS has a limited effect on it because $N = 1000$ elements are required before the path via the RIS becomes equally strong. Fig. 5 shows results with the ideal RIS configuration and the case with only four phase-shifts per element. The performance difference is small.

C. Reconfiguration under mobility

Most wireless channels are time-variant due to user mobility. Still, many properties of communication systems can be studied under the assumption that the channel is (approximately) piecewise time-invariant which allows employing LTI system theory, as done until this point. However, not all aspects can be analyzed in this manner. For example, the study of Doppler effects requires to drop the time-invariance assumption and employ linear time-variant (LTV) system theory.

We start by reconsidering the passband input-output relationship for an arbitrary system in (1), which is given by the convolution equation for LTV filters [25]:

$$y_{\text{pb}}(t) = \int_{-\infty}^{\infty} h_{\text{pb}}(u, t)x_{\text{pb}}(t - u)du \quad (35)$$

where $h_{\text{pb}}(\tau, t)$ is the real-valued time-varying impulse response which can be regarded as a conventional LTI channel impulse response in τ that is slowly varying with the time t . The time-variant transfer

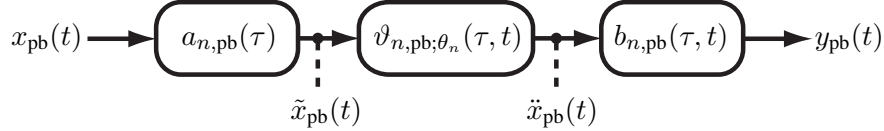


Fig. 6: The propagation path via the n th RIS element with three time-variant systems and two auxiliary signals.

function $H_{\text{pb}}(f, t)$ is defined as the continuous Fourier transform of $h_{\text{pb}}(\tau, t)$ with respect to τ :

$$H_{\text{pb}}(f, t) = \mathcal{F}_{c;\tau}\{h_{\text{pb}}(\tau, t)\} = \int_{-\infty}^{\infty} h_{\text{pb}}(\tau, t) e^{-j2\pi f\tau} d\tau. \quad (36)$$

This function could be regarded as a conventional LTI frequency response that is slowly varying with t . It connects the input and output of the system as

$$y_{\text{pb}}(t) = \mathcal{F}_{c;\tau}^{-1}\{H_{\text{pb}}(f, t)X_{\text{pb}}(f)\} = \int_{-\infty}^{\infty} H_{\text{pb}}(f, t)X_{\text{pb}}(f)e^{j2\pi ft}df. \quad (37)$$

Consider the example in Fig. 1 and assume that the receiver is a mobile terminal. Then, the uncontrollable channel $h_{d,\text{pb}}(\tau, t)$ and the controllable channels from the RIS elements to the receiver $b_{n,\text{pb}}(\tau, t)$, $n = 1, \dots, N$, are LTV filters. In contrast, the channels $a_{n,\text{pb}}(\tau)$, $n = 1, \dots, N$, are still LTI filters since the transmitter and the RIS are static. To analyze how the RIS can assist communication with mobile terminals, we need to drop the assumption that its configuration θ is constant during the transmission and consider it as an LTV filter with time-varying impulse response $\vartheta_{n,\text{pb};\theta_n}(\tau, t)$ and transfer function $\Theta_{n,\text{pb};\theta_n}(f, t)$.

The end-to-end propagation path over the n th RIS element is shown as a cascade of three systems in Fig. 6. Computing the joint impulse response for this path is slightly more complicated than before due to the cascade of two LTV filters. To this end, we define the auxiliary signals $\tilde{x}_{\text{pb}}(t)$ and $\ddot{x}_{\text{pb}}(t)$ as the output of the first and second filter in Fig. 6, respectively. It follows from (37) that

$$\ddot{x}_{\text{pb}}(t) = \int_{-\infty}^{\infty} \Theta_{n,\text{pb};\theta_n}(f, t)\tilde{X}_{\text{pb}}(f)e^{j2\pi ft}df \quad (38)$$

and, with (35), we obtain

$$y_{\text{pb}}(t) = \int_{-\infty}^{\infty} b_{n,\text{pb}}(u, t)\ddot{x}_{\text{pb}}(t-u)du \quad (39)$$

$$= \int_{-\infty}^{\infty} b_{n,\text{pb}}(u, t) \left(\int_{-\infty}^{\infty} \Theta_{n,\text{pb};\theta_n}(f, t-u)\tilde{X}_{\text{pb}}(f)e^{j2\pi f(t-u)}df \right) du \quad (40)$$

$$= \int_{-\infty}^{\infty} \left(\int_{-\infty}^{\infty} b_{n,\text{pb}}(u, t)\Theta_{n,\text{pb};\theta_n}(f, t-u)e^{-j2\pi fu}du \right) A_{n,\text{pb}}(f)X_{\text{pb}}(f)e^{j2\pi ft}df, \quad (41)$$

where the last step is because the channel from the transmitter to the RIS element is LTI. Comparing (41) to (37), we can identify the joint time-varying transfer function of the n th RIS propagation path as

$$H_{\text{pb};\theta_n}(f, t) = A_{n,\text{pb}}(f) \int_{-\infty}^{\infty} b_{n,\text{pb}}(u, t)\Theta_{n,\text{pb};\theta_n}(f, t-u)e^{-j2\pi fu}du. \quad (42)$$

The corresponding time-variant impulse response is $h_{\text{pb};\theta_n}(\tau, t) = \mathcal{F}_{c;\tau}^{-1}\{H_{\text{pb};\theta_n}(f, t)\}$. The time-varying end-to-end system impulse response, including the uncontrollable channel, then becomes

$$h_{\text{pb};\theta}(\tau, t) = h_{d,\text{pb}}(\tau, t) + \sum_{n=1}^N h_{\text{pb};\theta_n}(\tau, t). \quad (43)$$

For a narrowband channel with $A_{n,\text{pb}}(f) = \sqrt{\alpha_n}e^{-j2\pi f\tau_{n,a}}$ and $b_{n,\text{pb}}(\tau, t) = \sqrt{\beta_n(t)}\delta(\tau - \tau_{n,b}(t))$, we obtain from (42) the transfer function

$$H_{\text{pb};\theta_n}(f, t) = \sqrt{\alpha_n\gamma_{\theta_n}(t)\beta_n(t)}e^{-j2\pi f(\tau_{n,a} + \tau_{\theta_n}(t) + \tau_{n,b}(t))} \quad (44)$$

where we employed the time-varying RIS element transfer function $\Theta_{n,\text{pb};\theta_n}(f, t) = \sqrt{\gamma_{\theta_n}(t)}e^{-j2\pi f\tau_{\theta_n}(t)}$ obtained from (21) and utilized the fact that it can be arbitrarily translated in time. The joint channel impulse response is

$$h_{\text{pb};\theta}(\tau, t) = \sqrt{\rho(t)}\delta(\tau - \tau_d(t)) + \sum_{n=1}^N \sqrt{\alpha_n\gamma_{\theta_n}(t)\beta_n(t)}\delta(\tau - \tau_{n,a} - \tau_{\theta_n}(t) - \tau_{n,b}(t)). \quad (45)$$

Similar to (6), the received signal in the complex baseband system model becomes [23]

$$y(t) = \sqrt{\rho(t)}e^{-j2\pi f_c\tau_d(t)}x(t - \tau_d(t)) + \sum_{n=1}^N \sqrt{\alpha_n\gamma_{\theta_n}(t)\beta_n(t)}e^{-j2\pi f_c(\tau_{n,a} + \tau_{\theta_n}(t) + \tau_{n,b}(t))}x(t - \tau_{n,a} - \tau_{\theta_n}(t) - \tau_{n,b}(t)). \quad (46)$$

This system model allows to study the optimal RIS configuration taking mobility effects into account.

First, consider the case with only a controllable channel; that is, $\rho(t) = 0$ for all t . Recall from (30) that the capacity-maximizing configuration in this scenario is

$$\tau_{\theta_n}(t) = \varrho_n(t) - \tau_{n,a} - \tau_{n,b}(t) \quad (47)$$

for $\varrho_n(t)$ such that the received signal has the same phase over the N propagation paths. A valid choice is the delay-minimizing configuration with $\varrho_n(t) = \max_{i=1,\dots,N}\{\tau_{i,a} + \tau_{i,b}(t)\}$ for all n . While this is a constant when there is no mobility involved, it is a piecewise continuous function with possible jump discontinuities in time due to the pointwise maximum operation. This leads to phase jumps in the received signal and, hence, unwanted spectral effects. Avoiding these phase jumps requires restricting the phase-shifts induced by $\varrho_n(t)$ to integer multiples of 2π ; that is, $\varrho_n(t) = \frac{k_n(t)}{f_c}$ with $k_n(t)$ being a piecewise constant function taking integer values. Moreover, causality requires $\tau_{\theta_n}(t)$ to be nonnegative and, hence, $k_n(t) \geq f_c(\tau_{n,a} + \tau_{n,b}(t))$. Hence, the delay is minimized under these constraints by

$$k_n(t) = \max_{i=1,\dots,N} \lceil f_c(\tau_{i,a} + \tau_{i,b}(t)) \rceil \quad (48)$$

for all n . This increases the delay by at most one period of the carrier signal over the delay-minimizing configuration in (31) and does not introduce any delay spread.

Another phenomenon that only occurs under mobility is Doppler shift. For each propagation path, the Doppler shift is defined as the difference between the observed and emitted frequency:

$$\mathcal{D}_n = -\frac{d}{dt} [f_c (\tau_{n,a} + \tau_{\theta_n}(t) + \tau_{n,b}(t))] = -f_c \frac{d(\tau_{\theta_n}(t) + \tau_{n,b}(t))}{dt}. \quad (49)$$

Interestingly, the Doppler shift can be fully compensated for by the RIS by tuning the delays such that

$$\frac{d\tau_{\theta_n}(t)}{dt} = -\frac{d\tau_{n,b}(t)}{dt}. \quad (50)$$

This is known as Doppler cloaking and can help hide the movement of terminals. For the SNR and delay optimal configuration derived above, we obtain

$$\frac{d}{dt} \left(\frac{k_n(t)}{f_c} - \tau_{n,a} - \tau_{n,b}(t) \right) = \frac{1}{f_c} \frac{dk_n(t)}{dt} - \frac{d\tau_{n,b}(t)}{dt}. \quad (51)$$

Because changes in $k_n(t)$ do not lead to phase discontinuities, it has no effect on the Doppler shift and $\frac{dk_n(t)}{dt}$ can be assumed zero from a practical perspective. Hence, configuring the RIS according to (47) and (48) not only maximizes the SNR and minimizes the delay but also removes Doppler shifts [23].

Next, consider the case with an uncontrollable ‘‘direct’’ channel path (i.e., $\rho(t) \neq 0$), again under the assumption that it is shorter than the RIS path. Following (34), the SNR and delay optimal configuration is

$$\tau_{\theta_n}(t) = (\tau_d(t) - \tau_{n,a} - \tau_{n,b}(t)) + \frac{k_{n,\min}(t)}{f_c} \quad (52)$$

with $k_{n,\min}(t) = \lceil f_c (\tau_{n,a} + \tau_{n,b} - \tau_d) \rceil$. Using this configuration and employing (49), the Doppler shift of the propagation path over the n th RIS element is $\mathcal{D}_n = -f_c \frac{d}{dt} \tau_d(t)$, where we omitted $\frac{d}{dt} k_{n,\min}(t)$ for the same reason as before. This is the same as the Doppler shift of the uncontrollable channel and, hence, the Doppler spread is zero.

Note that it is impossible to simultaneously maximize the SNR and compensate for the Doppler shifts introduced by the RIS. However, even if this was possible, it would, most likely, not be the desired outcome as this would result in a Doppler spread of $f_c \frac{d}{dt} \tau_d(t)$. While a single Doppler shift can be compensated for quite easily, the Doppler spread is more challenging. Thus, having the RIS not introduce additional Doppler spread in the system could be considered the optimal solution in terms of Doppler effects.

In conclusion, we have observed that the SNR and delay optimal RIS configurations obtained using the developed LTI system model are also applicable under mobility and continue to be optimal in terms of the SNR. While some care has to be taken not to introduce additional frequency components into the spectrum due to phase discontinuities, an SNR-maximizing configuration also minimizes the delay spread and does not introduce additional Doppler spread into the system.

D. RIS design for wideband capacity maximization

The RIS optimization becomes more challenging in the wideband case where there are K parallel subcarriers, each represented by the system model in (17). The subcarriers are separate AWGN channels but share the power P since they are transmitted simultaneously. Suppose the power $P_\nu = \mathbb{E}\{|\bar{x}[\nu]|^2\}$ is assigned to subcarrier ν . Any power allocation P_0, \dots, P_{K-1} satisfying $P = \frac{1}{K} \sum_{\nu=0}^{K-1} P_\nu$ is feasible.

When studying this setup, we make use of the frequency response in (24) for the controllable channel via the RIS but we also add an uncontrollable channel. We let $\mathbf{h}_d = [h_d[0], \dots, h_d[M-1]]^T$ denote the discrete-time impulse response of the uncontrollable channel, which can be computed similar to (22): $h_d[k] = \sum_{l=1}^{L_d} \sqrt{\rho^l} e^{-j2\pi f_c \tau_d^l} \text{sinc}(k + B(\eta - \tau_d^l))$ where L_d is the number of paths, $\rho^l \in [0, 1]$ is propagation loss of the l th path, and $\tau_d^l \geq 0$ is its delay.

For a given RIS configuration $\boldsymbol{\theta}$ and power allocation, the so-called achievable rate is

$$R = \frac{B}{K + M - 1} \sum_{\nu=0}^{K-1} \log_2 \left(1 + \frac{P_\nu |\mathbf{f}_\nu^H \mathbf{h}_d + \mathbf{f}_\nu^H \mathbf{V}^T \boldsymbol{\omega}_\theta|^2}{BN_0} \right) \quad \text{bit/s} \quad (53)$$

where \mathbf{f}_ν^H is the ν th row of the DFT matrix \mathbf{F} . This rate expression is a summation over the K subcarriers, which is then divided by $K + M - 1$ (instead of K) to compensate for the cyclic prefix loss. The capacity is obtained by maximizing this expression with respect to both the power allocation and RIS configuration. The former is a classical problem with a solution called waterfilling power allocation [26]:

$$P_\nu = \max \left(\mu - \frac{BN_0}{|\mathbf{f}_\nu^H \mathbf{h}_d + \mathbf{f}_\nu^H \mathbf{V}^T \boldsymbol{\omega}_\theta|^2}, 0 \right) \quad (54)$$

where the parameter $\mu \geq 0$ is selected to make $\frac{1}{K} \sum_{\nu=0}^{K-1} P_\nu = P$.

The maximization of (53) with respect to the RIS configuration $\boldsymbol{\theta}$ entails selecting the most preferred vector $\boldsymbol{\omega}_\theta$ among those that the hardware can generate. Note that the same vector affects all subcarriers because the transmissions are simultaneous. In the narrowband case, we could optimize the RIS in closed form since there was only one channel (one subcarrier), but now we need to find a nontrivial tradeoff between all K subcarriers. So far, this problem seems mathematically intractable to solve to global optimality, thus the literature contains heuristic solutions based on successive convex approximation, semidefinite relaxation, and strongest tap maximization (STM) in the time domain [26]–[28]. In this article, we will focus on the STM solution from [27], [28] and compare it against an upper bound.

The intuition behind STM is that the received signal power is spread out over the K subcarriers but rather concentrated in the time domain since $M \ll K$ [27]. Hence, it is better to select a configuration $\boldsymbol{\theta}$ that is good for one channel tap than a configuration that is good for one subcarrier. This is particularly true when there is an LOS propagation path that is much stronger than all other paths. When adding the

uncontrollable channel to (23), the ℓ th tap of the impulse response becomes $h_d[\ell] + \mathbf{v}_\ell^T \boldsymbol{\omega}_\theta$. We begin by finding the value of $\boldsymbol{\omega}_\theta$ that maximizes the magnitude of each tap:

$$\boldsymbol{\omega}_\ell = \arg \max_{\boldsymbol{\omega}_\theta} |h_d[\ell] + \mathbf{v}_\ell^T \boldsymbol{\omega}_\theta|, \quad \ell = 0, \dots, M-1. \quad (55)$$

In STM, we then select the one of candidate solutions $\boldsymbol{\omega}_0, \dots, \boldsymbol{\omega}_{M-1}$ resulting in the largest magnitude:

$$\boldsymbol{\omega}_{\text{STM}} = \boldsymbol{\omega}_{\ell^{\text{opt}}} \quad \text{where} \quad \ell^{\text{opt}} = \arg \max_{\ell \in \{0, \dots, M-1\}} |h_d[\ell] + \mathbf{v}_\ell^T \boldsymbol{\omega}_\ell|. \quad (56)$$

Each of the subproblems in (55) can be solved analogously with the narrowband SNR maximization in (32). The solution is $\boldsymbol{\omega}_\ell = [e^{j(\arg(h_d[\ell]) - \arg([\mathbf{v}_\ell]_1))}, \dots, e^{j(\arg(h_d[\ell]) - \arg([\mathbf{v}_\ell]_N))}]^T$, where $[\mathbf{v}_\ell]_n$ denotes the n th entry of \mathbf{v}_ℓ and $\arg(\cdot)$ gives the argument (phase) of a complex number. Note that this solution rotates the phase of each term in the inner product $\mathbf{v}_\ell^T \boldsymbol{\omega}_\ell$ so it matches with the phase of $h_d[\ell]$.

To evaluate the quality of the heuristic STM solution, we can compare the rate that it achieves with an upper bound. Suppose we could select a different value of $\boldsymbol{\omega}_\theta$ on each subcarrier. We could then jointly maximize the SNRs of all subcarriers. For the ν th subcarrier, its SNR is maximized by selecting $\boldsymbol{\omega}_\theta = [e^{j(\arg(\mathbf{f}_\nu^H \mathbf{h}_d) - \arg([\mathbf{f}_\nu^H \mathbf{V}^T]_1))}, \dots, e^{j(\arg(\mathbf{f}_\nu^H \mathbf{h}_d) - \arg([\mathbf{f}_\nu^H \mathbf{V}^T]_N))}]^T$. The resulting upper bound is

$$R \leq \frac{B}{K + M - 1} \sum_{\nu=0}^{K-1} \log_2 \left(1 + \frac{P_\nu}{BN_0} (|\mathbf{f}_\nu^H \mathbf{h}_d| + \|\mathbf{f}_\nu^H \mathbf{V}^T\|_1)^2 \right) \quad (57)$$

where $\|\cdot\|_1$ denotes the L_1 norm. This upper bound is only practically achievable in the unlikely event that the same RIS configuration happens to maximize the SNRs of all subcarriers.

Fig. 7 shows simulation results for the achievable rates over a wideband channel, inspired by the setup in Fig. 1. The RIS and receiver are located in the same large room and, thus, have an LOS channel between them. The transmitter is an access point located 400 meters away and has an NLOS channel to the receiver. We will consider cases where the transmitter-to-RIS channel is either LOS or NLOS. The carrier frequency is 3 GHz and the RIS is 0.5×0.5 m, which corresponds to $N = 400$ elements that each have dimension $\lambda/4 \times \lambda/4$. The channels are modeled similar to the 3GPP channel model in [29] and the rate is averaged over random realizations of the multipath components. The rate in (53) is shown in Fig. 7 as a function of the bandwidth B . The optimal waterfilling power allocation from (54) is utilized and the transmit power P grows proportionally to the bandwidth. The subcarrier spacing is 150 kHz, thus the number of subcarriers increases with B as well as the number of channel taps.

Fig. 7(a) considers the case with an LOS path from the transmitter to the RIS. The dashed curve represents the rate when using the heuristic STM configuration of the RIS. It provides 96-98% of the upper bound from (57). The gap grows with B due to the increased frequency-selectivity, but since the LOS paths to/from the RIS are stronger than the scattered paths, it is possible to find a single RIS

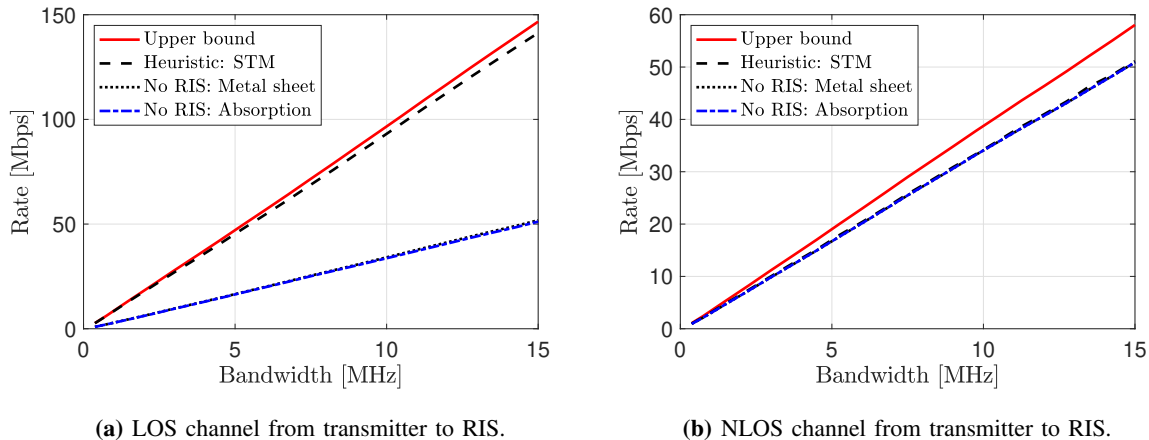


Fig. 7: The rate that can be achieved over a wideband channel grows proportionally to the bandwidth. If there are LOS channels to and from the RIS, it can greatly improve the slope and achieve a rate close to the upper bound in (57). This performance gain collapses if there is an NLOS path to the RIS.

configuration that works well over the entire band. The refined RIS configuration algorithms described in [26]–[28] can reduce the gap but only improve the rate by a few percent. It is interesting to compare the rate with what could be achieved without an RIS. In this case, we can either replace the RIS with an absorbing material, thereby removing all the paths via the RIS, or by a passive metal sheet causing zero phase-shifts. The corresponding curves in Fig. 7(a) are nearly overlapping but there are ideal situations where a perfectly rotated metal sheet is almost as efficient as an RIS [17]. The RIS can increase the rate by 2.7-2.9 times, which makes a huge difference when there are several MHz of bandwidth.

Fig. 7(b) considers the case with an NLOS path to the RIS, which has two effects: The path via the RIS is weaker and there is no dominant path. The former effect results in a much smaller gap between the upper bound and “no RIS” cases, while the latter results in an inability to find a single RIS configuration that fits the entire band. In this case, the RIS can improve the rate by 4% in the narrowband case of $B = 400$ kHz but the gain vanishes as B increases. One can find a slightly better RIS configuration using the algorithms in [26]–[28], but the bottomline is that an RIS must be carefully deployed to be truly effective. It should be deployed, as in Fig. 7(a), at a location with LOS to the access point and can then be configured to greatly improve the rate to users that are within LOS to it.

E. Protocol for channel estimation and reconfiguration

The capacity maximization has been described assuming that the channels are perfectly known, but a preceding channel estimation phase is required in practice. Since the RIS is passive, the estimation must be carried out at the receiver. If we focus on the OFDM case and neglect the uncontrollable channel, the

frequency response in (24) is $\bar{\mathbf{h}}_\theta = \mathbf{F}\mathbf{V}^\top\boldsymbol{\omega}_\theta$, where the matrix \mathbf{V} represents the cascade of the channel from the transmitter to the RIS and the channel from the RIS to the receiver. It is sufficient to estimate \mathbf{V} to compute $\bar{\mathbf{h}}_\theta$ for any $\boldsymbol{\omega}_\theta$, which is fortunate since it is hard to resolve the individual channels.

Suppose a known pilot signal x is transmitted on M subcarriers, where M is the number of (unknown) terms in the time-domain channel \mathbf{h}_θ . Let the RIS configuration be $\boldsymbol{\theta}_t$, where t is the index of the OFDM block. The received signal $\bar{\mathbf{z}}[t] \in \mathbb{C}^M$ over the M pilot-bearing subcarriers at OFDM block t is

$$\bar{\mathbf{z}}[t] = \mathbf{F}_M\mathbf{V}^\top\boldsymbol{\omega}_{\theta_t}x + \bar{\mathbf{w}}[t] \quad (58)$$

where \mathbf{F}_M contains the M rows of \mathbf{F} corresponding to the selected subcarriers and $\bar{\mathbf{w}}[t]$ contains the corresponding noise. There are MN unknown parameters in \mathbf{V} but we only obtain M observations from $\bar{\mathbf{z}}[t]$. Using more than M subcarriers for pilot transmission will not resolve this issue since the impact of the RIS configuration $\boldsymbol{\omega}_{\theta_t}$ cannot be removed from (58); a vector is non-invertible. The way to get MN linearly independent observations, where N is the number of RIS elements, is to consider a sequence of N OFDM blocks with different configurations: $\boldsymbol{\theta}_1, \dots, \boldsymbol{\theta}_N$. The joint received signal is

$$\underbrace{[\bar{\mathbf{z}}[1], \dots, \bar{\mathbf{z}}[N]]}_{=\bar{\mathbf{Z}}} = \mathbf{F}_M\mathbf{V}^\top \underbrace{[\boldsymbol{\omega}_{\theta_1}, \dots, \boldsymbol{\omega}_{\theta_N}]}_{=\boldsymbol{\Omega}} x + \underbrace{[\bar{\mathbf{w}}[1], \dots, \bar{\mathbf{w}}[N]]}_{=\bar{\mathbf{W}}}. \quad (59)$$

If the RIS configurations are selected such that $\boldsymbol{\Omega}$ is an invertible matrix, we can rewrite (59) as

$$\underbrace{\frac{1}{x}\mathbf{F}_M^{-1}\bar{\mathbf{Z}}\boldsymbol{\Omega}^{-1}}_{\text{Known signal}} = \mathbf{V}^\top + \underbrace{\frac{1}{x}\mathbf{F}_M^{-1}\bar{\mathbf{W}}\boldsymbol{\Omega}^{-1}}_{\text{Noise}}. \quad (60)$$

This is a linear model from which a variety of classical channel estimation techniques can be applied. In fact, (60) is already the least-square estimate of \mathbf{V}^\top . If there is prior information, such as a fading distribution or spatial-temporal sparsity, this can be used to devise better estimators [5]. One way to make $\boldsymbol{\Omega}$ invertible is to use a scaled DFT matrix [30]. Since switching between configurations is a non-linear operation and, thus, can modulate the reflected signals into other bands, it should be done in a silent guard interval in between OFDM blocks. After the receiver has estimated the channel, it can compute a suitable configuration $\boldsymbol{\omega}_\theta$ (as described earlier) that can be utilized as long as the channel remains static. The control channel described in Fig. 3 can be utilized to inform the RIS of the desired configuration. Since only M out of K subcarriers are used for pilots, the remaining ones can carry data. To handle mobility, one can develop protocols for progressive RIS reconfiguration where data is continuously transmitted and pilots are sent at regular intervals to re-estimate the channel and reconfigure the RIS [27], [28].

IV. RIS-AIDED LOCALIZATION AND SENSING

The objective of localization is to estimate and track the location of an actively communicating user device, while the objective of sensing is to estimate and track the location of passive objects or users. All

radio localization and sensing systems operate under common principles: there are location references, dynamic user states, and measurements, which are connected to the user state via a statistical model. The development of a radio localization system has three main components: design, channel estimation, and localization/sensing. *Design* includes the placement and configuration of reference points, and the design of pilot signals to maximize localization accuracy. The design can be offline, but also online, to adapt to current user location and requirements. An important tool in the design phase is Fisher information theory [31]. *Channel parameter estimation* is usually performed prior to localization and sensing, and involves estimation of geometric parameters (e.g., delays, angles, frequency shifts) from received signals. Note that both localization and communication rely on channel knowledge. However, localization explicitly determines the geometric parameters, while the unstructured channel (60) is sufficient for communication. *Location estimation, sensing, and tracking* are performed after channel estimation, with the aim to invert the geometric relation between the user's location and the channel parameter estimates to recover the user's location as well as the state of passive objects. Tracking algorithms (e.g., the extended Kalman filter) are used to recursively update these locations over time. Localization and sensing most often involve determination of nuisance parameters (e.g., synchronization and other biases, as well as data associations between measurements and objects), leading to high-dimensional and nonlinear optimization problems.

A. Localization and sensing in 4G and 5G

Each new generation of mobile communications introduces new features for higher-rate communication that also enable more accurate localization [32], as visualized in Fig. 8. In 4G systems, localization is based on the transmissions of pilot signals, sent by multiple synchronized base stations (BSs) over orthogonal subcarriers. The pilot design is such that it covers the entire signal bandwidth and avoids inter-BS interference. The user estimates the time-of-arrival (TOA) with respect to each BS, which depends on the distance to the BS and the user's clock bias. Estimating TOAs from at least four BSs in LOS allows the user to compute three time-difference-of-arrival (TDOA) measurements, and solve for its 3D location. The estimation accuracy depends on the SNR as well as the bandwidth spanned by the pilot signals, which determines the sampling rate and thereby the resolvability of the multipath components in time. In fact, multipath limits the accuracy to tens of meters in 4G [32]. In systems with a large bandwidth, the individual multipath components can be resolved and related to physical objects (e.g., a scatter point (SP)) in the environment [33].

In 5G systems operating in mmWave bands, the BS and possibly the user are equipped with multiple antennas [34]. The channel is then parameterized by both delays (as in 4G) and angles: angles-of-arrival (AOA) at the receiver and angles-of-departure (AOD) at the transmitter, both in azimuth and elevation.

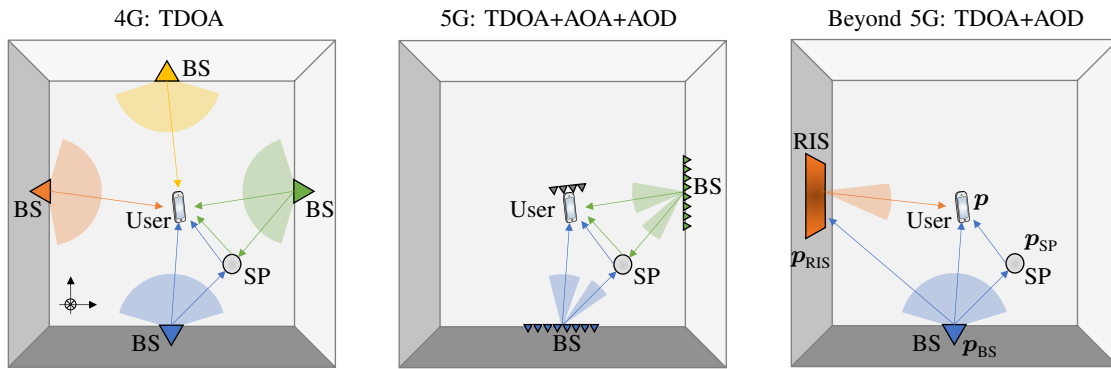


Fig. 8: Localization and sensing across generations of mobile communication technology: 4G relies on multiple BSs to obtain TDOA measurements. Uncontrollable multipath components (here represented by an SP) become a disturbance. In 5G, the inclusion of AOA and AOD measurements reduces the infrastructure needs and allows sensing of the environment. Beyond 5G, a scenario with a single BS and an RIS is shown. This infrastructure is sufficient to localize a user and provide partial map information, if we exploit that the RIS path is controllable.

This means that the user can be localized from the AOD of two BSs (by the intersection of two lines), significantly reducing infrastructure needs. The channel parameter measurements can be related to objects in the environment with unknown 3D locations through simultaneous localization and mapping (SLAM). In contrast to 4G, which must collect measurements over time [33], the additional angle measurements in 5G enable sensing of the environment from a single snapshot of observations [3], [35].

B. Localization and sensing with an RIS

The inclusion of an RIS provides several new opportunities for localization [8], [36]. They are new synchronized location references and configurable for optimizing localization performance. Each RIS also leads to several new geometric measurements, which in turn improves localization accuracy and coverage. The 5G scenario in Fig. 8 is easily generalized to a scenario with an RIS [37], making the problem highly over-determined and in a sense easier. Thus, we will focus on the more refined and challenging case with one single-antenna transmitting BS, one single-antenna receiving user, and one RIS with N elements. While communication uses approximately sinc-shaped pulses, localization uses approximately square-shaped pulses. Suppose the uncontrollable channel from the transmitter (i.e., BS) to the receiver (i.e., UE) consists of L_d propagation paths, where $\rho^l \in [0, 1]$ is the propagation loss and $\tau_d^l \geq 0$ is the delay of the l th path. The first one is the LOS path. Furthermore, the RIS is in the far-field and there is only an LOS path to/from the RIS (i.e., $L_a = L_b = 1$) where τ_{RIS} denotes the propagation delay via the first element. Under these circumstances, if $\bar{x} \in \mathbb{C}^K$ is the transmitted pilot signal over the K subcarriers, the received signal $\bar{z}[t]$ in the OFDM block with index t is

$$\bar{z}[t] = \underbrace{\sum_{l=1}^{L_d} g^l \mathbf{d}(\tau_d^l) \odot \bar{\mathbf{x}}}_{\text{Uncontrollable channel}} + \underbrace{\mathbf{v}^T \boldsymbol{\omega}_\theta (\mathbf{d}(\tau_{\text{RIS}}) \odot \bar{\mathbf{x}})}_{\text{Controllable channel}} + \bar{\mathbf{w}}[t] \quad (61)$$

where \odot is the Hadamard product, $g^l = \sqrt{\rho^l} e^{-j2\pi f_c \tau_d^l}$ is the complex channel gain of path l . Here $\mathbf{d}(\tau) \in \mathbb{C}^K$ with $[\mathbf{d}(\tau)]_\nu = e^{-j2\pi\tau\Delta_f\nu}$ where $\Delta_f = B/K$ is the subcarrier spacing. The vectors $\mathbf{v} \in \mathbb{C}^N$ and $\boldsymbol{\omega}_\theta \in \mathbb{C}^N$ are defined in (23). Due to the far-field assumption, we have $\alpha_n = \alpha$ and $\beta_n = \beta$, for all n , and we can make use of the steering vector of the RIS, which we call $\mathbf{a}(\phi) \in \mathbb{C}^N$ where $\phi = [\phi^{\text{az}}, \phi^{\text{el}}]^T \in \mathbb{R}^2$ contains the azimuth and elevation angle. The steering vector gives the phase-shifts between the RIS elements for a plane wave impinging from ϕ . If we further assume that the fraction of re-radiated power from all RIS elements is identical, i.e., $\gamma_{\theta_n} = \gamma$ in $\boldsymbol{\omega}_\theta$, we can write $\mathbf{v}^T \boldsymbol{\omega}_\theta$ in (61) as

$$\mathbf{v}^T \boldsymbol{\omega}_\theta = g_{\text{RIS}} \left(\underbrace{\mathbf{a}(\phi_a) \odot \mathbf{a}(\phi_b)}_{=\mathbf{b}(\phi_b)} \right)^T \bar{\boldsymbol{\omega}}_\theta \quad (62)$$

where $g_{\text{RIS}} = \sqrt{\alpha\beta\gamma} e^{j\psi_{\text{RIS}}}$ with ψ_{RIS} being a global phase-shift and $\phi_a = [\phi_a^{\text{az}}, \phi_a^{\text{el}}]^T \in \mathbb{R}^2$ and $\phi_b = [\phi_b^{\text{az}}, \phi_b^{\text{el}}]^T \in \mathbb{R}^2$ are the (azimuth and elevation) AOA and AOD at the RIS, respectively. The vector $\bar{\boldsymbol{\omega}}_\theta \in \mathbb{C}^N$ is obtained from $\boldsymbol{\omega}_\theta$ by setting $\gamma_n = 1$ for all n and, thus, has entries on the unit circle. If the geographical locations $\mathbf{p}_{\text{BS}} \in \mathbb{R}^3$ and $\mathbf{p}_{\text{RIS}} \in \mathbb{R}^3$ of the BS and RIS, respectively, are known, so is the AOA ϕ_a and we use the notation $\mathbf{b}(\phi_b) = \mathbf{a}(\phi_a) \odot \mathbf{a}(\phi_b)$ in (62) to focus on the unknown angle ϕ_b .

In the system model above, there are $3L_d + 5$ real unknown parameters: $L_d + 1$ complex channel gains $\{g_{\text{RIS}}, g^l : l = 1, \dots, L_d\}$, $L_d + 1$ delays $\{\tau_{\text{RIS}}, \tau_d^l : l = 1, \dots, L_d\}$, and a two-dimensional AOD vector ϕ_b . Let $\mathbf{p} \in \mathbb{R}^3$ denote the unknown user location and $\mathbf{p}_{\text{SP},l} \in \mathbb{R}^3$ denote the location of the l th SP, for $l = 2, \dots, L_d$. These location parameters are related to the system model parameters as follows:

$$\tau_d^1 = \|\mathbf{p}_{\text{BS}} - \mathbf{p}\|/c + \Delta_{\text{clk}}, \quad (63)$$

$$\tau_d^l = \|\mathbf{p}_{\text{BS}} - \mathbf{p}_{\text{SP},l}\|/c + \|\mathbf{p}_{\text{SP},l} - \mathbf{p}\|/c + \Delta_{\text{clk}}, \quad l > 1, \quad (64)$$

$$\tau_{\text{RIS}} = \|\mathbf{p}_{\text{BS}} - \mathbf{p}_{\text{RIS}}\|/c + \|\mathbf{p} - \mathbf{p}_{\text{RIS}}\|/c + \Delta_{\text{clk}}, \quad (65)$$

$$\phi_b^{\text{az}} = \arctan2([\mathbf{R}^T(\mathbf{p} - \mathbf{p}_{\text{RIS}})]_2, [\mathbf{R}^T(\mathbf{p} - \mathbf{p}_{\text{RIS}})]_1), \quad (66)$$

$$\phi_b^{\text{el}} = \arccos([\mathbf{R}^T(\mathbf{p} - \mathbf{p}_{\text{RIS}})]_3 / \|\mathbf{p} - \mathbf{p}_{\text{RIS}}\|), \quad (67)$$

where $\Delta_{\text{clk}} \in \mathbb{R}$ is the user's clock bias, c is the speed of light, $\mathbf{R} \in \mathbb{C}^{3 \times 3}$ is the rotation matrix defining the RIS's orientation (i.e., $\mathbf{R}^T \mathbf{z}$ maps \mathbf{z} from the global to the local RIS coordinate system), and $[z]_n$ is the n th entry of \mathbf{z} . Signal amplitudes may also be used in localization [38] but this is not explored here.

Without an RIS, estimating \mathbf{p} from (61) is impossible since the observation only yields $L_d - 1$ TDOA measurements $\{\tau_d^l - \tau_d^1 : l = 2, \dots, L_d\}$, while there are $3L_d$ unknown geometric parameters: the user

location \mathbf{p} and the locations of the $L_d - 1$ scatter points $\mathbf{p}_{\text{SP},l}$ (after removal of the clock bias). However, we will show that adding a single RIS to the setup is sufficient to make the problem identifiable in terms of \mathbf{p} , though not $\mathbf{p}_{\text{SP},l}$. In particular, we will see the RIS acts as an additional synchronized BS with an analog array. We will describe the localization subproblems in detail: design (offline RIS placement, online RIS configuration), channel parameter estimation (determining $\{\tau_{\text{RIS}}, \phi_b, \tau_d^l : l = 1, \dots, L_d\}$), localization and synchronization (determining \mathbf{p} and Δ_{clk}), and sensing (determining $\{\mathbf{p}_{\text{SP},l} : l = 2, \dots, L_d\}$).

RIS configuration encoding: In localization, propagation paths with similar geometric parameters (angles or delays) will not be resolved when two conditions are met: (i) the delays and angles are similar; and (ii) they are correlated. Non-resolved paths can lead to large biases in the estimates of angles and delays. Making the RIS configuration $\bar{\mathbf{w}}_\theta$ time-varying provides new dimensions to make paths resolvable. This can be achieved as follows over T transmission blocks. We use a number $Q \ll T$ RIS configurations $\bar{\mathbf{w}}_{\theta_1}, \dots, \bar{\mathbf{w}}_{\theta_Q}$ and associate a unique code (e.g., a column from a DFT matrix) $\mathbf{c} = [c_1, \dots, c_{T/Q}]^T \in \mathbb{C}^{T/Q}$, $|c_n| = 1$ with a temporal balance property $\mathbf{c}^T \mathbf{1} = 0$. The actual RIS configuration is $c_t \bar{\mathbf{w}}_{\theta_i}$. The switching is done in silent intervals between OFDM blocks to avoid modulating the reflected signals to other bands. The received signal with to the i th configuration is

$$\bar{\mathbf{z}}^{(i)}[t] = \sum_{l=1}^{L_d} g^l \mathbf{d}(\tau_d^l) \odot \bar{\mathbf{x}} + c_t g_{\text{RIS}} \mathbf{b}^T(\phi_b) \bar{\mathbf{w}}_{\theta_i} (\mathbf{d}(\tau_{\text{RIS}}) \odot \bar{\mathbf{x}}) + \mathbf{w}^{(i)}[t], \quad t = 1, \dots, T/Q \quad (68)$$

where we use the same range of time indices for all configurations and separate them using the index i . The observations are grouped as $\mathbf{Z}^{(i)} = [\bar{\mathbf{z}}^{(i)}[1], \dots, \bar{\mathbf{z}}^{(i)}[T/Q]]$, from which we can compute an observation of the uncontrolled channel as $\hat{\mathbf{z}}^{(0)} = \sum_{i=1}^Q \mathbf{Z}^{(i)} \mathbf{1}$ (with processing gain T) and of the i th configuration of the controlled channel as $\hat{\mathbf{z}}^{(i)} = \mathbf{Z}^{(i)} \mathbf{c}^*$ (with processing gain T/Q). This principle significantly reduces complexity and storage at the RIS, and is easy to generalize to a multi-RIS setup.

C. RIS design for localization and sensing

We want to design an RIS-enabled localization system in a deployment region $\mathcal{R} \subset \mathbb{R}^3$. We will rely on Fisher information theory (as developed for wideband localization in [31], which we use as a basis in this article) for both offline and online design. We denote the unknown channel parameters as

$$\boldsymbol{\zeta} = [\tau_d^1, \tau_{\text{RIS}}, \phi_b^T, \boldsymbol{\tau}_{l>1}^T, \mathbf{g}^T, g_{\text{RIS}}]^T. \quad (69)$$

where $\boldsymbol{\tau}_{l>1} = [\tau_d^2, \tau_d^3, \dots, \tau_d^{L_d}]^T$ and $\mathbf{g} = [g^1, g^2, \dots, g^{L_d}]^T$. The design parameter vector $\boldsymbol{\sigma}$ accounts for the placement and configuration of the RIS and is selected from a set \mathcal{S} . The Fisher information matrix (FIM) can then be defined as

$$\mathbf{J}(\boldsymbol{\zeta}|\boldsymbol{\sigma}) = \frac{2}{N_0} \sum_{t=1}^T \Re \{ (\nabla_{\boldsymbol{\zeta}} \boldsymbol{\mu}[t])^H \nabla_{\boldsymbol{\zeta}} \boldsymbol{\mu}[t] \}, \quad (70)$$

where $\boldsymbol{\mu}[t] = \bar{\mathbf{z}}[t] - \bar{\mathbf{w}}[t]$ is the noise-free observation, $\nabla_{\boldsymbol{\zeta}}\boldsymbol{\mu}[t] \in \mathbb{C}^{K \times (3L_a + 5)}$ denotes the gradient, and \Re returns the real part of its argument. The FIM satisfies the fundamental Fisher information inequality $\mathbf{J}^{-1}(\boldsymbol{\zeta}|\boldsymbol{\sigma}) \preceq \mathbb{E}\{(\boldsymbol{\zeta} - \hat{\boldsymbol{\zeta}})(\boldsymbol{\zeta} - \hat{\boldsymbol{\zeta}})^T\}$ (in the positive semidefinite sense), under certain technical conditions, for any unbiased estimator $\hat{\boldsymbol{\zeta}}$ of the channel parameters. We define a corresponding parameter vector in the location domain $\tilde{\boldsymbol{\zeta}} = [\mathbf{p}, \Delta_{\text{clk}}, \boldsymbol{\tau}_{l>1}^T, \mathbf{g}^T, g_{\text{RIS}}]^T$ and associated Jacobian $\boldsymbol{\Upsilon} = \nabla_{\tilde{\boldsymbol{\zeta}}}\boldsymbol{\zeta}$, so that $\mathbf{J}(\tilde{\boldsymbol{\zeta}}|\boldsymbol{\sigma}) = \boldsymbol{\Upsilon}^T \mathbf{J}(\boldsymbol{\zeta}|\boldsymbol{\sigma}) \boldsymbol{\Upsilon}$. From $\mathbf{J}(\tilde{\boldsymbol{\zeta}}|\boldsymbol{\sigma})$, we can finally compute the FIM of the user location using Schur's complement: we partition $\mathbf{J}(\tilde{\boldsymbol{\zeta}}|\boldsymbol{\sigma}) = [\mathbf{A} \ \mathbf{B}; \ \mathbf{B}^T \ \mathbf{C}]$, where $\mathbf{A} \in \mathbb{R}^{3 \times 3}$ so that $\mathbf{J}(\mathbf{p}|\boldsymbol{\sigma}) = \mathbf{A} - \mathbf{B}\mathbf{C}^{-1}\mathbf{B}^T$. When $\mathbf{J}(\mathbf{p}|\boldsymbol{\sigma})$ is invertible, we say that the location is identifiable with $\mathbf{J}^{-1}(\mathbf{p}|\boldsymbol{\sigma}) \preceq \mathbb{E}\{(\mathbf{p} - \hat{\mathbf{p}})(\mathbf{p} - \hat{\mathbf{p}})^T\}$. Since the FIM is a matrix, it is inconvenient as a design metric. However, the squared position error bound (SPEB) is a meaningful scalar metric (measured in m^2)

$$\text{SPEB}(\mathbf{p}|\boldsymbol{\sigma}) = \text{trace}(\mathbf{J}^{-1}(\mathbf{p}|\boldsymbol{\sigma})) \leq \mathbb{E}\{\|\mathbf{p} - \hat{\mathbf{p}}\|^2\}. \quad (71)$$

1) *Offline design for optimized coverage:* A reasonable criterion for the offline design phase is to provide uniform coverage or to maximize the fraction of the deployment region with low SPEB. The latter criterion can be expressed as

$$\underset{\boldsymbol{\sigma} \in \mathcal{S}}{\text{maximize}} \quad \frac{1}{|\mathcal{R}|} \int_{\mathcal{R}} \mathbb{I}\{\text{SPEB}(\mathbf{p}|\boldsymbol{\sigma}) \leq \varepsilon^2\} \, d\mathbf{p} \quad (72)$$

where \mathbb{I} is an indicator function, $|\mathcal{R}|$ is the size of the deployment region, and ε is a required accuracy (e.g., 1 m). Solving for $\boldsymbol{\sigma}$ leads to the optimal placement of the RIS. The problem (72) can be solved by an exhaustive search over a finite set \mathcal{S} ignoring the uncontrolled channel, except for the LOS path, and using random RIS configurations $\bar{\boldsymbol{\omega}}_{\theta_i}$.

2) *Online design for optimized localization performance:* During the online design phase, we possibly have a priori information of the location of the users and the origins of the uncontrolled channel. The online problem to minimize worst-case localization performance is then of the form

$$\underset{\boldsymbol{\sigma} \in \mathcal{S}}{\text{minimize}} \quad \max_{\mathbf{p}} \text{SPEB}(\mathbf{p}|\boldsymbol{\sigma}) \quad (73)$$

where $\boldsymbol{\sigma}$ includes the RIS configuration $\bar{\boldsymbol{\omega}}_{\theta}$. The inner maximization $\max_{\mathbf{p}}$ is over the high-probability region of the user location. This problem can be rewritten as

$$\begin{aligned} & \underset{\boldsymbol{\sigma} \in \mathcal{S}, \mathbf{u}}{\text{minimize}} \quad \mathbf{u}^T \mathbf{1} \\ & \text{subject to} \quad \begin{bmatrix} \mathbf{J}(\tilde{\boldsymbol{\zeta}}|\boldsymbol{\sigma}) & \mathbf{e}_k \\ \mathbf{e}_k^T & u_k \end{bmatrix} \succeq \mathbf{0}, \quad k = 1, 2, 3, \quad \forall \tilde{\boldsymbol{\zeta}}, \end{aligned} \quad (74)$$

where \mathbf{e}_k is a vector of zeros, except for a 1 in the k th entry, and constraints are added for each probable value of $\tilde{\boldsymbol{\zeta}}$. The problem (74) is convex when the variable $\boldsymbol{\sigma}$ appears linearly in $\mathbf{J}(\tilde{\boldsymbol{\zeta}}|\boldsymbol{\sigma})$. The designs that

minimize the SPEB are generally different from those that maximize communication-centric metrics such as the capacity: though both have better performance at higher SNR, the localization accuracy depends also on the geometry and ability to separate, rather than align, signals from different paths.

D. Algorithms for localization and sensing

The algorithmic design depends on the underlying channel estimation method, as well as the specific scenario. The algorithms can be Bayesian (i.e., providing a characterization of the distribution of the user and SP locations) or non-Bayesian (providing only a point estimate). A complete overview of such methods is out of the scope of this article. Instead, we focus on single-antenna transmitters/receivers defined in (61).

1) *Algorithms for channel parameter estimation:* The controlled and uncontrolled channels can be separated using the balanced code described in (68). We obtain the following observation of the uncontrolled channel:

$$\hat{\mathbf{z}}^{(0)} = \sum_{i=1}^Q \mathbf{Z}^{(i)} \mathbf{1} = T \sum_{l=1}^{L_d} g^l \mathbf{d}(\tau_d^l) \odot \bar{\mathbf{x}} + \sum_{t=1}^T \sum_{i=1}^Q \mathbf{w}^{(i)}[t]. \quad (75)$$

Similarly, for the i th configuration in the controlled channel ($i \in \{1, \dots, Q\}$), we observe:

$$\hat{\mathbf{z}}^{(i)} = \mathbf{Z}^{(i)} \mathbf{c}^* = \frac{T}{Q} g_{\text{RIS}} \mathbf{b}^T(\phi_b) \bar{\omega}_{\theta_i} (\mathbf{d}(\tau_{\text{RIS}}) \odot \bar{\mathbf{x}}) + \sum_{t=1}^T \mathbf{w}^{(i)}[t] c_t^*. \quad (76)$$

Estimation of the uncontrolled channel can be performed using any standard channel estimation technique, e.g., compressive sensing [39]. Estimation of the controlled channel involves only a single path (note that multi-bounce reflections are very weak and hard to detect) and can be performed using techniques from multi-antenna channel estimation [40].

2) *Algorithms for localization and sensing:* After channel estimation, the interface towards localization and sensing is via the estimated geometric channel parameters, say $\{\hat{\tau}_d^l : l = 1, \dots, L_d\}$, $\hat{\tau}_{\text{RIS}}$, and $\hat{\phi}_b$. In the absence of a priori information, localization and sensing is usually performed by determining an initial guess, based on the geometric relations, followed by a refinement based on the likelihood function, which itself depends on the underlying channel estimation method.

- *Localization:* Assuming the LOS delay can be identified (e.g., from the large path power), (63) and (65) leads a TDOA measurement, which defines a hyperbola with respect to the user position \mathbf{p} :

$$(\hat{\tau}_{\text{RIS}} - \hat{\tau}_d^1)c \approx \|\mathbf{p} - \mathbf{p}_{\text{RIS}}\| + \|\mathbf{p}_{\text{BS}} - \mathbf{p}_{\text{RIS}}\| - \|\mathbf{p} - \mathbf{p}_{\text{BS}}\|, \quad (77)$$

while measurements of the AOD in (66)–(67) determine a line from the RIS with direction

$$\mathbf{k}(\hat{\phi}_b) \approx \frac{\mathbf{R}^T(\mathbf{p} - \mathbf{p}_{\text{RIS}})}{\|\mathbf{R}^T(\mathbf{p} - \mathbf{p}_{\text{RIS}})\|}. \quad (78)$$

The intersection of the hyperbola with the line determines the user location, say $\hat{\mathbf{p}}$. An example will be provided later in Fig. 11. Substituting $\hat{\mathbf{p}}$ back into (63) provides us with an estimate of the clock bias, say $\hat{\Delta}_{\text{clk}}$. We note that in the presence of two RISs, the delay measurement is not even needed, opening a path for accurate localization over narrowband channels. These estimates can be refined with gradient descent on the likelihood function.

- *Sensing*: After the user location is determined, the sources of uncontrolled channel can be constrained by

$$(\hat{\tau}_d^l - \hat{\tau}_d^1)c + \|\hat{\mathbf{p}} - \mathbf{p}_{\text{BS}}\| \approx \|\hat{\mathbf{p}} - \mathbf{p}_{\text{SP},l}\| + \|\mathbf{p}_{\text{BS}} - \mathbf{p}_{\text{SP},l}\|, \quad l > 1. \quad (79)$$

The right-hand side can be interpreted as a time-sum-of-arrival (TSOA), which determines an ellipse with the BS and estimated user location as focal points. Since the controlled channel from the RIS is not dependent on the uncontrolled channel, the RIS does not directly improve sensing, but rather indirectly through better localization accuracy. Note that when there is detectable multi-bounce multipath (BS to RIS to SP to the user), then the AOD from the RIS to the SP can also be inferred, allowing unique localization of each SP.

E. Indoor localization example

We will now illustrate the localization in a 2D scenario, where the elevation angle ϕ_b^{el} is removed from the set of unknown parameters to simplify the exposition. Following the scenario from Fig. 8, we consider a 10 m \times 10 m indoor environment with the BS in the middle of a wall at location $\mathbf{p}_{\text{BS}} = [0, 0]^T$. An RIS can be placed in the center of each of the three remaining walls. The BS has an antenna that is omnidirectional in the azimuth plane and operates at $f_c = 28$ GHz with 400 MHz bandwidth using $K = 3000$ subcarriers and a transmission power of 20 dBm. The RIS comprises $N = 64$ elements deployed along a line with $\lambda/5$ spacing (e.g., the total size is about 14 cm) and unity per-element gain $G(\phi^{\text{az}}) = 1$ for $|\phi^{\text{az}}| \leq \pi/2$ and $G(\phi^{\text{az}}) = 0$ elsewhere. The noise power spectral density is $N_0 = -174$ dBm/Hz. We use $Q = 8$ RIS configurations and $T = 256$ transmission blocks. The pilot symbols have constant modulus. We generate

$$g^1 = \frac{\lambda}{4\pi\|\mathbf{p} - \mathbf{p}_{\text{BS}}\|} e^{j\psi^1}, \quad (80)$$

$$g^l = \frac{\lambda\sqrt{\sigma_{\text{RCS}}}}{(4\pi)^{3/2}} \frac{1}{\|\mathbf{p} - \mathbf{p}_{\text{SP},l}\|} \frac{1}{\|\mathbf{p}_{\text{SP},l} - \mathbf{p}_{\text{BS}}\|} e^{j\psi^l}, \quad l > 1 \quad (81)$$

$$g_{\text{RIS}} = \sqrt{G(\phi_a^{\text{az}})G(\phi_b^{\text{az}})} \frac{(\lambda/5)^2}{4\pi} \frac{1}{\|\mathbf{p}_{\text{RIS}} - \mathbf{p}_{\text{BS}}\|} \frac{1}{\|\mathbf{p}_{\text{RIS}} - \mathbf{p}\|} e^{j\psi_{\text{RIS}}} \quad (82)$$

where $\psi^l, \psi_{\text{RIS}}$ are independently and uniformly distributed in $[0, 2\pi)$, while σ_{RCS} is the radar cross section (RCS) of the SP, expressed in m^2 .

1) *FIM analysis*: It is instructive to investigate $\mathbf{J}(\mathbf{p}|\boldsymbol{\sigma})$ deeper for the fundamental case without uncontrolled multipath (only LOS) and a single RIS. Using RIS configurations with temporal balance and balanced power allocation across subcarriers and an RIS phase reference in the center of the RIS, the FIM of the geometric parameters $[\tau_d^1, \tau_{\text{RIS}}, \phi_b^{\text{az}}]^T$ is a diagonal matrix with entries (see [31, Eq. (16)–(17)] and [41, Eq. (4)])

$$J(\tau_d^1) = \frac{2|g^1|^2}{N_0} T B_{\text{eff}}^2 \quad (83)$$

$$J(\tau_{\text{RIS}}) = \frac{2\|g_{\text{RIS}}\|^2 \|\bar{\mathbf{x}}\|^2 T}{N_0 Q} B_{\text{eff}}^2 \sum_{i=1}^Q |\mathbf{b}^T(\phi_b^{\text{az}}) \bar{\boldsymbol{\omega}}_{\theta_i}|^2 \quad (84)$$

$$J(\phi_b^{\text{az}}) = \frac{2\|g_{\text{RIS}}\|^2 \|\bar{\mathbf{x}}\|^2 T}{N_0 Q} \left(\sum_{i=1}^Q |\dot{\mathbf{b}}^T(\phi_b^{\text{az}}) \bar{\boldsymbol{\omega}}_{\theta_i}|^2 - \frac{|\sum_{i=1}^Q (\mathbf{b}^T(\phi_b^{\text{az}}) \bar{\boldsymbol{\omega}}_{\theta_i}) (\dot{\mathbf{b}}^T(\phi_b^{\text{az}}) \bar{\boldsymbol{\omega}}_{\theta_i})^*|^2}{\sum_{i=1}^Q |\mathbf{b}^T(\phi_b^{\text{az}}) \bar{\boldsymbol{\omega}}_{\theta_i}|^2} \right) \quad (85)$$

where $B_{\text{eff}}^2 = \sum_{k=1}^K (2\pi k \Delta_f)^2 |\bar{x}_k|^2$ and $\dot{\mathbf{b}}(\phi_b^{\text{az}})$ denotes the derivative of $\mathbf{b}(\phi_b^{\text{az}})$ with respect to ϕ_b^{az} . Based on the Jacobian, it is can be verified that the FIM becomes

$$\mathbf{J}(\mathbf{p}|\boldsymbol{\sigma}) = \frac{1}{c^2} \frac{J(\tau_d^1) J(\tau_{\text{RIS}})}{J(\tau_d^1) + J(\tau_{\text{RIS}})} (\mathbf{u}_{\text{BS}} - \mathbf{u}_{\text{RIS}})(\mathbf{u}_{\text{BS}} - \mathbf{u}_{\text{RIS}})^T + J(\phi_b^{\text{az}}) \frac{\boldsymbol{\Xi} \mathbf{u}_{\text{RIS}} \mathbf{u}_{\text{RIS}}^T \boldsymbol{\Xi}^T}{\|\mathbf{p}_{\text{RIS}} - \mathbf{p}\|^2}, \quad (86)$$

where $\boldsymbol{\Xi} = [0 \ -1; +1 \ 0]$ is a rotation matrix over $\pi/2$, \mathbf{u}_{BS} is a unit vector from the BS to the user and \mathbf{u}_{RIS} a unit vector from the RIS to the user. The expression (86) shows that with aid of the RIS, we obtain two fundamental directions of Fisher information: one according to $\mathbf{u}_{\text{BS}} - \mathbf{u}_{\text{RIS}}$, with intensity (as defined in [31]) that depends on the TOA accuracy of both the LOS and RIS path, and one orthogonal to \mathbf{u}_{RIS} , with an intensity reduced with the distance. This FIM analysis provides contradictory design requirements: for optimal TOA estimation we should maximize the SNR and set $\bar{\boldsymbol{\omega}}_{\theta_i} = \mathbf{b}^*(\phi_b^{\text{az}})$, for all i . This is equivalent to the solution found in (31) that maximizes capacity, but leads to $J(\phi_b^{\text{az}}) = 0$, meaning that the AOD cannot be estimated. On the other hand, for optimal AOD estimation (85) indicates that $\bar{\boldsymbol{\omega}}_{\theta_i}$ should be a combination of $\mathbf{b}^*(\phi_b^{\text{az}})$ and $\dot{\mathbf{b}}(\phi_b^{\text{az}})$. Hence, a natural compromise is to configure the RIS using $\bar{\boldsymbol{\omega}}_{\theta_i} = \mathbf{b}^*(\phi_b^{\text{az}})$ for a fraction of the available transmissions, and set $\bar{\boldsymbol{\omega}}_{\theta_i} \approx \dot{\mathbf{b}}^*(\phi_b^{\text{az}})$ for the remaining transmissions (which involves approximating the derivative beam to be generated by the RIS so that $|\bar{\boldsymbol{\omega}}_{\theta_i}|_n = 1$). By optimizing the fraction, the two terms in (86) can be balanced. The RIS essentially behaves like an additional synchronized BS equipped with a phased array.

2) *Offline design*: We first consider five alternative designs: no RIS, an RIS on the left wall, an RIS on the front wall (facing the BS), an RIS on the right wall, or three RISs (one on each remaining wall, using orthogonal temporally balanced codes). Random RIS phase configurations were assumed. The objective function defined in (72) with $\varepsilon = 0.1$ m is equal to 0, 0.35, 0.45, 0.35 and 0.99, respectively. This shows

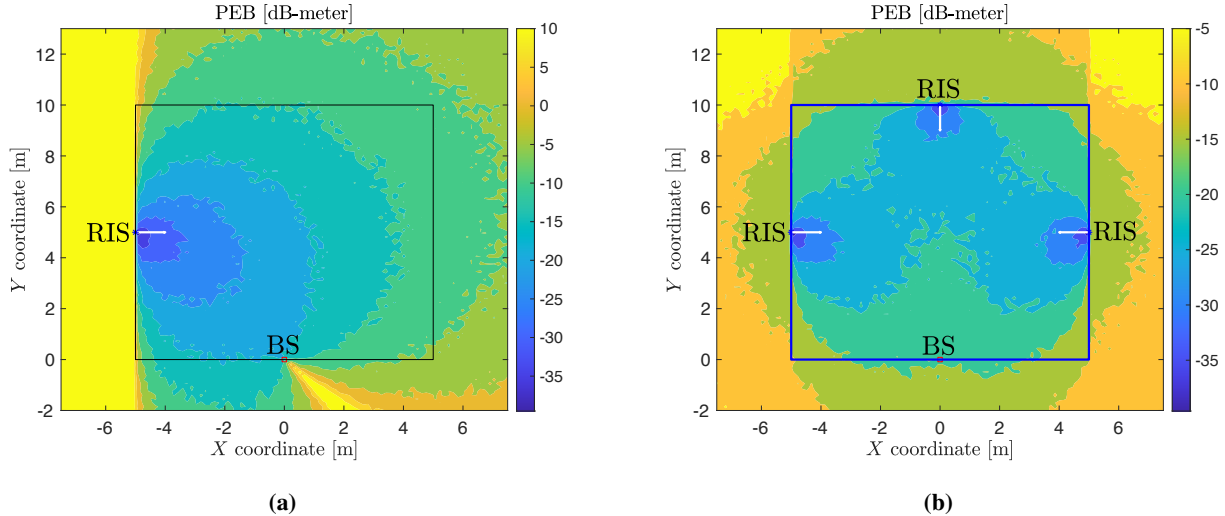


Fig. 9: Offline design: (a) shows the PEB (in dB-meter) over space for one RIS and (b) for three RISs. Note that $\varepsilon = 0.1$ m corresponds to -10 dB-meter. White lines show the direction of the RIS (normal to the RIS).

that it is better to put the RIS on the far wall (despite larger propagation loss), and that using three RISs can provide uniform coverage in the deployment region. To gain further insight, Fig. 9 shows a contour plot of $\text{PEB}(\mathbf{x}|\boldsymbol{\sigma}) = \sqrt{\text{SPEB}(\mathbf{x}|\boldsymbol{\sigma})}$ for two of the configurations $\boldsymbol{\sigma}$ (RIS on the left wall and three RISs). We see that when an RIS is placed on the left wall, low PEB is achieved only very close to the RIS, especially in the lower part of the room, closer to the BS. Along the line between the BS and RIS, behind the BS, the PEB tends to infinity, since $\mathbf{u}_{\text{BS}} - \mathbf{u}_{\text{RIS}} = \mathbf{0}$, so the TDOA measurement brings no information. Behind the RIS, the PEB is also infinite, due to the zero per-element gain $G(\phi^{\text{az}})$. On the other hand, with three RISs, we can obtain acceptable performance throughout the deployment region.

3) *Online design:* We now use a single RIS on the left wall (see Fig. 9a) and a user at $\mathbf{p} = [-3, 8]^T$. We aim to optimize the RIS configuration for this location and consider the following alternatives (which describe the set \mathcal{S} of design variables): (i) set $\bar{\boldsymbol{\omega}}_{\theta_i}$ to be random, $i = 1, \dots, 8$, each configuration is used 32 times; (ii) in the $T = 256$ transmissions, use T_1 times the direct beam configuration $\bar{\boldsymbol{\omega}}_{\theta_i} = \mathbf{b}^*(\phi_b^{\text{az}})$ and $T - T_1$ times the approximation of the derivative beam configuration $\bar{\boldsymbol{\omega}}_{\theta_i} \approx \dot{\mathbf{b}}^*(\phi_b^{\text{az}})$. In Fig. 10, we evaluate, as a function of T_1/T , the $\text{PEB}(\mathbf{p}|\boldsymbol{\sigma})$, the error standard deviation of $c\tau_{\text{RIS}}$, $c\sqrt{J^{-1}(\tau_{\text{RIS}})}$; and the error standard deviation of ϕ_b^{az} , given by $\sqrt{J^{-1}(\phi_b^{\text{az}})}$. We recall that $T_1 = T$ is optimal in terms of SNR and TOA estimation accuracy. However, from a localization perspective, the best performance is achieved when $T_1/T \approx 0.63$, while for $T_1 = 0$ and $T_1 = T$, the PEB diverges. The behavior can be explained by inspecting the TOA and AOD performance: a large T_1 leads to high SNR and maximizes $J(\tau_{\text{RIS}})$, so the best TOA estimation from the RIS is achieved when only $\bar{\boldsymbol{\omega}}_{\theta_i} = \mathbf{b}^*(\phi_b^{\text{az}})$ is used. However,

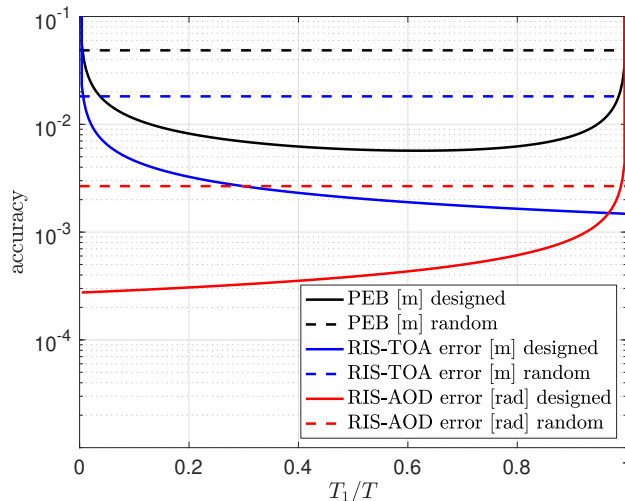


Fig. 10: Online design of the RIS configuration for a specific user location: performance as a function of the fraction T_1/T of configurations that maximizes the SNR over the total number of configurations. Performance with random RIS configurations is shown as a reference.

in that case, $J(\phi_b^{az}) \rightarrow 0$ so that the measurement does not provide any information about the AOD from the RIS. While not obvious from the figure, when only $\bar{\omega}_{\theta_i} \approx \dot{\mathbf{b}}^*(\phi_b^{az})$ is sent, $J(\tau_{\text{RIS}}) = J(\phi_b^{az}) = 0$, since $\mathbf{b}^T(\phi_b^{az})\dot{\mathbf{b}}^*(\phi_b^{az}) = 0$. The random configurations (though providing information when there is no prior on the user's location) lead to worse PEB performance than the optimally designed configurations.

4) *Localization and sensing:* As a final example, we again use a single RIS on the left wall, a user at $\mathbf{p} = [-3, 8]^T$, and an SP at location $\mathbf{p}_{\text{SP}} = [3, 4]^T$ with RCS of $\sigma_{\text{RCS}} = 1 \text{ m}^2$. To estimate the delays of the uncontrolled channel, we apply a DFT to (75) and determine the peaks. These can then be converted to $\hat{\tau}_d^1$ and $\hat{\tau}_d^2$. To estimate the TOA and AOD from the controlled channel, we use (76) and perform a 2D search over $[\tau_{\text{RIS}}, \phi_b^{az}]$ with a substituted estimate of the channel gain. This yields $\hat{\tau}_{\text{RIS}}$ and $\hat{\phi}_b$. Fig. 11 shows the locations of the BS, user, RIS, and SP, the TDOA hyperbola from (77) as well as the AOD bearing line from (78). Their intersection is the estimated location $\hat{\mathbf{p}}$. From this estimated location and the TOA of the uncontrolled channel, we obtain a TSOA ellipse (79), near which the SP must lie. Note that from a snapshot, the SP location cannot be determined, but after sufficient movement of the user and appropriate data association, the SP location can be uniquely identified.

F. Conclusions from RIS-aided localization

An RIS can be seen as a synchronized multi-antenna BS with a phased array that can aid the localization. Proper placement of the RIS can provide significant location coverage improvements, even

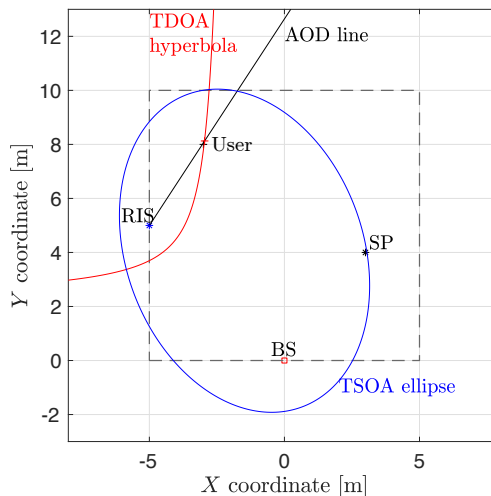


Fig. 11: Localization and sensing example, based on the outputs of the channel estimation. The user location is estimated based on the LOS and controlled channel. Finally, the SP can be constrained to be on an ellipse.

in a setup with a single-antenna user and BS. The RIS configuration can be tailored to the specific user location, but is significantly different from the optimal configuration for communications. This is also reflected by the different simulation setups considered in this article: many RIS elements are required in communications to improve the end-to-end SNR, while localization requires large bandwidths but the RIS can be small since it is primarily used to add new dimensions to resolve identifiability issues. An increase in the number of RIS elements can enable the use of less bandwidth. Moreover, while for communication, the RIS provides limited gains when the LOS path is present, for localization both paths provide useful and necessary information. In addition, by encoding the RIS configurations with a global code, the controlled and uncontrolled channels can be separated, and multiple non-interfering RISs can be supported. The use of RIS for sensing is mainly indirect, by the improved estimation of the user location, provided the uncontrolled and controlled channels do not interact.

V. FUNDAMENTAL ELECTROMAGNETIC PROPERTIES AND SIGNAL PROCESSING CHALLENGES

We next elaborate on a few fundamental phenomena that appear when having a large and dense RIS. By refining the models to capture these properties, there are opportunities to develop new signal processing algorithms that push the boundaries of how communications and localization are normally conceived.

A. Scaling laws and near-field regime

The benefit of classical beamforming from an antenna array is that the SNR grows linearly with the number of antennas N [1]. When maximizing the narrowband capacity, we noticed that the SNR with an RIS instead grows as $N^2\alpha\beta\gamma$, when the N paths have the same propagation loss. The quadratic SNR

scaling does not mean that the setup in Fig. 1 can achieve a higher SNR than in a case where the RIS is replaced by an equal-sized antenna array that is transmitting with equal power. In the latter case, the SNR would be proportional to $N\beta$. To understand the difference, we can factorize the SNR scaling achieved by the RIS as $(N\alpha\gamma) \cdot (N\beta)$. The first term accounts for the fraction of the transmitter's signal power that is reflected by the RIS, which is a very small number even when N is large since $\alpha < -70$ dB is typical. Hence, the RIS cannot achieve a higher SNR than $N\beta$ but the difference reduces as $1/N$. When comparing an RIS with alternative technologies, the RIS must be physically larger to be competitive [5].

SNR scaling behaviors are extensively studied in signal processing for communications and localization to understand the ultimate performance and obtain intuitive performance approximations for cases with large arrays. Although the asymptotic regime where $N \rightarrow \infty$ is commonly studied, practical technologies have thus far operated far from the limit so it has been unimportant whether the underlying models are asymptotically accurate or not. Since the law of conservation of energy dictates that we cannot receive more power than what was transmitted, there must be a finite upper bound on the SNR even when $N \rightarrow \infty$. The aforementioned SNR scalings were obtained under the classical far-field assumption: the N RIS elements experience roughly the same propagation loss. However, when the transmitter and/or receiver is at a distance from the RIS that is at the same order as the RIS's width/height, the RIS elements experience large differences in propagation loss due to the varying propagation distances and angles [21]. This scenario is unavoidable as $N \rightarrow \infty$ but also occurs in practice when the RIS is 1 m wide and the user is at a similar distance. By modeling the geometric near-field properties, one can derive how the SNR converges to a finite upper limit [21]. More importantly, the near-field enables the RIS to focus signals not only in a particular direction but at a certain point in that direction, thereby making the RIS better than a mirror [5]. This property can also be utilized for improved localization [37]. Since classical array signal processing focuses on the far-field, there are great opportunities to develop new algorithms that exploit the unique near-field properties for improved communication and localization.

B. Spatial degrees-of-freedom

In a multipath environment, different parts of the RIS will observe different linear combinations of the impinging waves, leading to fading variations. The wavelength sets a limit on the variability and, even in cases with rich scattering, there will be a correlation between the channel coefficients observed at RIS elements that are up to a few wavelengths apart [42]. This fundamental property has several impacts on the RIS operation. The inherent sparsity can be exploited to simplify the channel estimation. It can be used to mitigate fading variations over the end-to-end link since these are likely to average out when the surface is large. It also enables an RIS to reflect multiple signals to different locations simultaneously,

thereby enabling communication or localization with multiple users. There are signal processing research challenges in both channel modeling, algorithmic design, and optimization.

C. *Non-linear RIS operation*

This article focuses on applications where the RIS has a (piecewise) constant configuration, in which case it can be modeled as a linear filter. We also explained how linear time-variant system theory can be used in the case where the RIS is tuned to mitigate the Doppler effect caused by mobility. A different option is to vary the RIS configuration continuously during the transmission of a signal block to modulate the transmitted signal before it is reradiated [43]. This effectively creates a non-linear end-to-end channel where the received signal contains a wider range of frequencies than the transmitted signal. The key applications remain to be discovered but it is clear that signal processing provides the right tools for analysis and optimization.

D. *Mutual coupling*

A model assumption that was made already in Fig. 1 is that the N elements act as separate filters that each take a single input. However, when the RIS elements are closely spaced, it is hard to fully isolate them on the substrate material. This leads to mutual coupling where the impedance of one element is connected with the impedances of the neighboring elements. Hence, if Fig. 2 exemplifies how an RIS element behaves in isolation, in reality, the frequency response will vary depending on the configuration of the neighboring elements. The mutual impedance is dependent on the physical properties of the elements and can be determined through lengthy full-wave simulations, such as the method of moments, that must be carried out for each configuration. Such an analysis has previously been done for antenna arrays. The special case of canonical minimum-scattering (CMS) antennas [44] allows expressing the mutual impedance as a closed-form function of the distance and orientations of two antennas [45]–[47].

The CMS approach does however not capture the desired operation of the RIS as CMS antennas do not allow full 2π phase control [48]. In contrast, an RIS made from patch or slot antennas effectively decouples the amplitude and phase of the reflected wave, allowing full 2π phase control. Without proper modeling of the mutual impedance, the trade-off between complexity and performance as the RIS is densified cannot be evaluated. As such, different modeling techniques that do not rely on the CMS assumption has to be developed to capture the behavior of RISs with closely spaced elements.

For conventional antenna arrays, mutual coupling carries drawbacks such as scan blindness and ohmic losses. Scan blindness is when the wave is fully reflected and might be a desirable effect for an RIS.

The high ohmic losses of superdirectivity could potentially be utilized to absorb interference as heat. As such, these effects present themselves as new opportunities that should be reevaluated in the RIS context.

A methodology based on circuit theory can be utilized to develop discrete-time RIS system models that capture mutual coupling, but this research is yet in its infancy. Mutual coupling will have an impact on the algorithmic design as well as the communication/localization performance. If accurate models are hard to develop, machine learning methods might be useful to address the problem of system identification.

VI. SUMMARY

This article has provided a tutorial of the basic system modeling of wireless signaling that involves RIS. This emerging technology can be utilized to increase the capacity of communication systems and the accuracy of localization and sensing systems. While the same models underpin both applications, the preferred embodiments differ in terms of bandwidth requirements, RIS dimensions, and optimal configuration. The basic algorithms and properties have been described in this article, but there is a goldmine of open signal processing problems, for example, related to refined models capturing the relevant electromagnetic properties, experimental validation, and more realistic applications. Since RIS technology is often mentioned in 6G research, *now is the right time* to explore these open problems.

VII. ACKNOWLEDGMENTS

We would like to thank Gonzalo Seco-Granados, Kamran Keykhosravi, Özlem Tugfe Demir, and Robin J. Williams for their comments and feedback during the writing.

REFERENCES

- [1] B. D. V. Veen and K. M. Buckley, "Beamforming: a versatile approach to spatial filtering," *IEEE ASSP Mag.*, vol. 5, no. 2, pp. 4–24, 1988.
- [2] E. Björnson, L. Sanguinetti, H. Wymeersch, J. Hoydis, and T. L. Marzetta, "Massive MIMO is a reality—What is next? Five promising research directions for antenna arrays," *Digital Signal Processing*, vol. 94, pp. 3–20, Nov. 2019.
- [3] K. Witrals, P. Meissner, E. Leitinger, Y. Shen, C. Gustafson, F. Tufvesson, K. Haneda, D. Dardari, A. F. Molisch, A. Conti, and M. Z. Win, "High-accuracy localization for assisted living: 5G systems will turn multipath channels from foe to friend," *IEEE Signal Process. Mag.*, vol. 33, no. 2, pp. 59–70, 2016.
- [4] O. Tsilipakos *et al.*, "Toward intelligent metasurfaces: The progress from globally tunable metasurfaces to software-defined metasurfaces with an embedded network of controllers," *Advanced Optical Materials*, no. 2000783, 2020.
- [5] E. Björnson, Ö. Özdoğan, and E. G. Larsson, "Reconfigurable intelligent surfaces: Three myths and two critical questions," *IEEE Commun. Mag.*, no. 12, pp. 90–96, 2020.
- [6] C. Liaskos, S. Nie, A. Tsioliaridou, A. Pitsillides, S. Ioannidis, and I. Akyildiz, "A new wireless communication paradigm through software-controlled metasurfaces," *IEEE Commun. Mag.*, vol. 56, no. 9, pp. 162–169, 2018.

- [7] M. D. Renzo *et al.*, “Smart radio environments empowered by reconfigurable intelligent surfaces: How it works, state of research, and road ahead,” *IEEE J. Sel. Areas Commun.*, vol. 38, no. 11, pp. 2450–2525, 2020.
- [8] H. Wymeersch, J. He, B. Denis, A. Clemente, and M. Juntti, “Radio localization and mapping with reconfigurable intelligent surfaces: Challenges, opportunities, and research directions,” *IEEE Veh. Technol. Mag.*, vol. 15, no. 4, pp. 52–61, 2020.
- [9] M. D. Renzo *et al.*, “Smart radio environments empowered by reconfigurable AI meta-surfaces: an idea whose time has come,” *EURASIP J. Wirel. Commun. Netw.*, vol. 2019:129, 2019.
- [10] P. Popovski, *Wireless Connectivity: An Intuitive and Fundamental Guide*. Wiley, 2020.
- [11] Q. Wu, S. Zhang, B. Zheng, C. You, and R. Zhang, “Intelligent reflecting surface aided communications: A tutorial,” *CoRR*, vol. abs/2007.02759v2, 2020.
- [12] C. Huang, A. Zappone, G. C. Alexandropoulos, M. Debbah, and C. Yuen, “Reconfigurable intelligent surfaces for energy efficiency in wireless communication,” *IEEE Trans. Wireless Commun.*, vol. 18, no. 8, pp. 4157–4170, 2019.
- [13] J. Huang, *Reflectarray Antenna*. John Wiley & Sons, Inc., 2005.
- [14] S. V. Hum and J. Perruisseau-Carrier, “Reconfigurable reflectarrays and array lenses for dynamic antenna beam control: A review,” *IEEE Trans. Antennas Propag.*, vol. 62, no. 1, pp. 183–198, 2014.
- [15] P. Nayeri, F. Yang, and A. Z. Elsherbeni, “Beam-scanning reflectarray antennas: A technical overview and state of the art,” *IEEE Antennas Propag. Mag.*, vol. 57, no. 4, pp. 32–47, 2015.
- [16] B. Zhu, J. Zhao, and Y. Feng, “Active impedance metasurface with full 360° reflection phase tuning,” *Scientific Reports*, vol. 3, no. 3059, 2013.
- [17] Ö. Özdoğan, E. Björnson, and E. G. Larsson, “Intelligent reflecting surfaces: Physics, propagation, and pathloss modeling,” *IEEE Wireless Commun. Lett.*, vol. 9, no. 5, pp. 581–585, 2020.
- [18] Q. Wu and R. Zhang, “Towards smart and reconfigurable environment: Intelligent reflecting surface aided wireless network,” *IEEE Commun. Mag.*, vol. 58, no. 1, pp. 106–112, 2020.
- [19] S. Abeywickrama, R. Zhang, Q. Wu, and C. Yuen, “Intelligent reflecting surface: Practical phase shift model and beamforming optimization,” *IEEE Trans. Commun.*, vol. 68, no. 9, pp. 5849–5863, 2020.
- [20] M. Di Renzo *et al.*, “Reconfigurable intelligent surfaces vs. relaying: Differences, similarities, and performance comparison,” *IEEE Open J. Commun. Soc.*, vol. 1, pp. 798–807, 2020.
- [21] E. Björnson and L. Sanguinetti, “Power scaling laws and near-field behaviors of massive MIMO and intelligent reflecting surfaces,” *IEEE Open J. Commun. Soc.*, vol. 1, pp. 1306–1324, 2020.
- [22] Q. Wu and R. Zhang, “Intelligent reflecting surface enhanced wireless network via joint active and passive beamforming,” *IEEE Trans. Wireless Commun.*, vol. 18, no. 11, pp. 5394–5409, 2019.
- [23] B. Matthiesen, E. Björnson, E. D. Carvalho, and P. Popovski, “Intelligent reflecting surface operation under predictable receiver mobility: A continuous time propagation model,” *IEEE Wireless Commun. Lett.*, 2020.
- [24] Q. Wu and R. Zhang, “Beamforming optimization for wireless network aided by intelligent reflecting surface with discrete phase shifts,” *IEEE Trans. Commun.*, vol. 68, no. 3, pp. 1838–1851, 2020.
- [25] R. G. Gallager, *Principles of Digital Communication*. Cambridge University Press, 2008.
- [26] Y. Yang, B. Zheng, S. Zhang, and R. Zhang, “Intelligent reflecting surface meets OFDM: Protocol design and rate maximization,” *IEEE Trans. Commun.*, vol. 68, no. 7, pp. 4522–4535, 2020.
- [27] B. Zheng and R. Zhang, “Intelligent reflecting surface-enhanced OFDM: Channel estimation and reflection optimization,” *IEEE Wireless Commun. Lett.*, vol. 9, no. 4, pp. 518–522, 2020.
- [28] S. Lin, B. Zheng, G. C. Alexandropoulos, M. Wen, F. Chen, and S. Mumtaz, “Adaptive transmission for reconfigurable

- intelligent surface-assisted OFDM wireless communications,” *IEEE J. Sel. Areas Commun.*, vol. 38, no. 11, pp. 2653–2665, 2020.
- [29] *Spatial channel model for Multiple Input Multiple Output (MIMO) simulations (Release 16)*. 3GPP TS 25.996, Jul. 2020.
- [30] T. L. Jensen and E. De Carvalho, “An optimal channel estimation scheme for intelligent reflecting surfaces based on a minimum variance unbiased estimator,” in *IEEE ICASSP*, 2020, pp. 5000–5004.
- [31] Y. Shen and M. Z. Win, “Fundamental limits of wideband localization—part I: A general framework,” *IEEE Trans. Inf. Theory*, vol. 56, no. 10, pp. 4956–4980, 2010.
- [32] J. A. del Peral-Rosado, R. Raulefs, J. A. López-Salcedo, and G. Seco-Granados, “Survey of cellular mobile radio localization methods: From 1G to 5G,” *IEEE Commun. Surveys Tuts.*, vol. 20, no. 2, pp. 1124–1148, 2017.
- [33] E. Leitinger, F. Meyer, F. Hlawatsch, K. Witrisal, F. Tufvesson, and M. Z. Win, “A belief propagation algorithm for multipath-based SLAM,” *IEEE Trans. Wireless Commun.*, vol. 18, no. 12, pp. 5613–5629, 2019.
- [34] R. M. Buehrer, H. Wymeersch, and R. M. Vaghefi, “Collaborative sensor network localization: Algorithms and practical issues,” *Proc. IEEE*, vol. 106, no. 6, pp. 1089–1114, 2018.
- [35] Y. Ge, F. Wen, H. Kim, M. Zhu, F. Jiang, S. Kim, L. Svensson, and H. Wymeersch, “5G SLAM using the clustering and assignment approach with diffuse multipath,” *Sensors*, vol. 20, no. 16, p. 4656, 2020.
- [36] A. Bourdoux *et al.*, “6G white paper on localization and sensing,” *6G Research Visions*, vol. 12, 2020.
- [37] A. Elzanaty, A. Guerra, F. Guidi, and M.-S. Alouini, “Reconfigurable intelligent surfaces for localization: Position and orientation error bounds,” *arXiv preprint arXiv:2009.02818*, 2020.
- [38] H. Zhang, H. Zhang, B. Di, K. Bian, Z. Han, and L. Song, “Towards ubiquitous positioning by leveraging reconfigurable intelligent surface,” *IEEE Commun. Lett.*, vol. 25, no. 1, pp. 284–288, 2020.
- [39] K. Venugopal, A. Alkhateeb, N. G. Prelcic, and R. W. Heath, “Channel estimation for hybrid architecture-based wideband millimeter wave systems,” *IEEE J. Sel. Areas Commun.*, vol. 35, no. 9, pp. 1996–2009, 2017.
- [40] A. Fascista, A. Coluccia, H. Wymeersch, and G. Seco-Granados, “Millimeter-wave downlink positioning with a single-antenna receiver,” *IEEE Trans. Wireless Commun.*, vol. 18, no. 9, pp. 4479–4490, 2019.
- [41] N. Garcia, H. Wymeersch, and D. T. M. Slock, “Optimal precoders for tracking the AoD and AoA of a mmWave path,” *IEEE Trans. Signal Process.*, vol. 66, no. 21, pp. 5718–5729, 2018.
- [42] E. Björnson and L. Sanguinetti, “Rayleigh fading modeling and channel hardening for reconfigurable intelligent surfaces,” *IEEE Wireless Commun. Lett.*, 2021, to appear.
- [43] J. Yuan, E. D. Carvalho, R. J. Williams, E. Björnson, and P. Popovski, “Frequency-mixing intelligent reflecting surfaces for nonlinear wireless propagation,” *CoRR*, 2021. [Online]. Available: <http://arxiv.org/abs/2007.01085>
- [44] W. Wasylkiwskyj and W. K. Kahn, “Theory of mutual coupling among minimum-scattering antennas,” *IEEE Trans. Antennas Propag.*, vol. 18, no. 2, pp. 204–216, 1970.
- [45] M. T. Ivrlac and J. A. Nosssek, “Toward a circuit theory of communication,” *IEEE Trans. Circuits Syst. I*, vol. 57, no. 7, pp. 1663–1683, 2010.
- [46] G. Gradoni and M. Di Renzo, “End-to-end mutual-coupling-aware communication model for reconfigurable intelligent surfaces: An electromagnetic-compliant approach based on mutual impedances,” Sep. 2020. [Online]. Available: <http://arxiv.org/abs/2009.02694>
- [47] R. J. Williams, P. Ramírez-Espinosa, E. de Carvalho, and T. L. Marzetta, “Multiuser MIMO with large intelligent surfaces: Communication model and transmit design,” 2020. [Online]. Available: <http://arxiv.org/abs/2011.00922>
- [48] X. Qian and M. Di Renzo, “Mutual Coupling and Unit Cell Aware Optimization for Reconfigurable Intelligent Surfaces,” *arXiv:2011.14373 [cs, math]*, Nov. 2020, arXiv: 2011.14373. [Online]. Available: <http://arxiv.org/abs/2011.14373>